UCONN LIBRARY

University of Connecticut
OpenCommons@UConn

Doctoral Dissertations | University of Connecticut Graduate School

5-11-2017

Combined Intrinsic Caloric Effects in Ferroelectrics

Hamidreza Khassaf
Ph.D. Candidate, hamidreza.khassaf@uconn.edu

Follow this and additional works at: https://opencommons.uconn.edu/dissertations

Recommended Citation
Khassaf, Hamidreza, "Combined Intrinsic Caloric Effects in Ferroelectrics" (2017). *Doctoral Dissertations*. 1382.
https://opencommons.uconn.edu/dissertations/1382

Combined Intrinsic Caloric Effects in Ferroelectrics

Hamidreza Khassaf

University of Connecticut, 2017

There exist multiple driving forces in solid–state materials that can be utilized for entropy changes and hence stronger caloric response. In multiferroic materials, adiabatic temperature changes (ΔT_{ad}) can be obtained by the combined application of electric, stress, and magnetic fields. These external stimuli provide additional channels of entropy variations resulting in a multi–caloric response. In ferroelectric (FE) materials, caloric responses can be obtained with the application of electric and mechanical fields. Here, we compute the intrinsic electrocaloric and elastocaloric of prototypical FE materials using Landau–Devonshire theory of phase transformations with appropriate electrical and electro–mechanical boundary conditions. Also, the flexocaloric response of FE material systems are computed due to generation of strain gradient induced misfit dislocations. Our electrocaloric calculations indicate that the intrinsic ΔT_{ad} in relaxor FEs are substantial and do not vary much over a large temperature interval. Also, we show that an elastocaloric ΔT_{ad} of 12.7 ◦C can be obtained in $PbTiO_3$ with the application of uniaxial tensile stress of 500 MPa near its Curie point. Moreover, flexocaloric ΔT_{ad} exceeding 1.81 °C can be realized in 20 nm thick barium titanate films. We show a strong link between strain relaxation and strain gradients in epitaxial films and their caloric response. These findings indicate that caloric responses in ferroic materials can be deterministically controlled and enhanced by utilizing a variety of external stimuli. Our results suggest a promising perspective to find solid–state systems with giant caloric responses to be used as alternatives for conventional refrigeration technologies.

Combined Intrinsic Caloric Effects in Ferroelectrics

Hamidreza Khassaf

M.Sc., Sabanci University, 2012

B.Sc., Amirkabir University of Technology (Tehran Polytechnic), 2010

A Dissertation

Submitted in Partial Fulfillment of the

Requirements for the Degree of

Doctor of Philosophy

at the

University of Connecticut

2017

Copyright by
Hamidreza Khassaf

2017

APPROVAL PAGE

Doctor of Philosophy Dissertation

Combined Intrinsic Caloric Effects in Ferroelectrics

Presented by

Hamidreza Khassaf, M.Sc.

Major Advisor_____

Dr. S. Pamir Alpay

Associate Advisor_____

Dr. Mark Aindow

Associate Advisor_____

Dr. Serge M. Nakhmanson

Associate Advisor_____

Dr. Puxian Gao

Associate Advisor_____

Dr. Seok–Woo Lee

University of Connecticut

2017

ACKNOWLEDGEMENTS

First of all, I would like to thank my Ph.D. advisor, Dr. S. Pamir Alpay. I have received full and heartwarming support from him throughout my studies and I very much appreciate his guidance. I also want to thank my advisory committee, Drs. Mark Aindow, Serge M. Nakhmanson, Puxian Gao, and Seok–Woo Lee for all the useful discussions we have had during my studies. I would like to thank my office– and lab–mates Nasser Khakpash, Dr. Sanjeev K. Nayak, Tulsi Patel, Mehmet Tumerkan Kesim, Dr. Fu–Chang Sun, Dr. Peiman Shahbeigi–Roodposhti, Yomery Espinal, John Mangery, Dr. Sanjubala Sahoo, Dr. Vinit Sharma, Dr. Jialan Zhang, Thomas Reid, Denis Trujillo, Kevin Co, Dr. Liang Dong, Dr. Ching–Chang Chung, and Dr. Richard Perez–Moyet. They have all been considerate, knowledgeable, and very kind to me of which I am grateful. I would like to thank my parents Aliakbar Khassaf and Sima Rayga for all their support and encouragement. I have misses them so much in the past five years and I hope us being apart comes to an end in a near future. And finally, I am very much grateful to have given the chance to meet my lovely wife Bahareh Mahrou at UConn. Giving me the chance to know her is by far, the best thing that UConn did for me.

TABLE OF CONTENTS

APPROVAL PAGE III
ACKNOWLEDGEMENTS IV
TABLE OF CONTENTS V
LIST OF FIGURES VII
LIST OF TABLES X
CHAPTER 1: INTRODUCTION 1
SOLID–STATE CALORIC EFFECT 1
FERROELECTRICITY 4
COUPLING BETWEEN MECHANICAL, ELECTRICAL, AND THERMAL PROPERTIES IN FES 7
Thermodynamic Formulation 9
THERMODYNAMICS OF FERROELECTRICS 11
OBJECTIVES OF THE THESIS 12
CHAPTER 2: CALORIC EFFECTS IN FERROELECTRICS 13
ELECTROCALORIC EFFECT 14
Polarization, Heat Capacity, and Pyroelectric Coefficient 16
Adiabatic Temperature Change 18
Analyzing the Electrocaloric Effect 21
Materials and Methods 23
Details of Theoretical Methodology 23
Experimental Details 25
Electrocaloric Effect: Summary 26
MECHANOCALORIC EFFECT 27
Definitions and Importance 27
Theoretical Approach 30
Elastocaloric Response 33
Stress Mediated Electrocaloric Response (Hydrostatic Pressure) 37
Discussion & Concluding Remarks 39
FLEXOCALORIC EFFECT 42
Introduction of Flexoelectric Effect 42
Flexoelectric Effect in Epitaxial Thin–Films 43
Flexocaloric Effect in Epitaxially Strained Thin Films 45
Misfit Dislocations and Flexocaloric Calculations 45
Concluding Remarks 56

CHAPTER 4: SUMMARY AND CONCLUTSION 57
Electrocaloric Response in Ferroelectric Materials 58
Mechanocaloric Response in Ferroelectric Materials 59
Flexocaloric Response in Ferroelectric Materials 59
REFERENCES 61

LIST OF FIGURES

Figure 1– Various aspects of optimization of caloric responces in ferroelectric material systems: They include: reversibility, temperature and entropy changes, temperature span of applicability, filed strengths, hysteresis losses, cost and environmental concerns 2

Figure 2– Structural paraelectric–ferroelectric phase transition: The structure changes from a centrosymmetrical cubic paraelectric phase to a non–centrosymmetrical tetragonal ferroelectric phase. The illustrated phases are perovskite structures where green, blue, and red spheres are anions, cations, and oxygen ions, respectively. 4

Figure 3– Change of (a) polarization and (b) dielectric constant of stress–free monodomain uniaxial barium titanate with temperature at various electric fields 6

Figure 4– (a) Pyroelectric effect: a change in the temperature results in a variation in the polarization that generates a pyroelectric current; (c) Electrocaloric effect: A change in the applied electric field from E_a to E_b generates an electric field change ΔE that results in an adiabatic temperature variation ΔT_{ad}. 7

Figure 5– Coupling between mechanical, electrical, and thermal properties in FEs 9

Figure 6– Direct and coupling physical effects and corresponding thermodynamic relations 10

Figure 7– Polarization variations of barium titanate as functions of temperature and electric field: First order phase transition smears as the electric field is applied (a) and a ferroelectric hysteresis loop starts to shape up once the temperature decreases to $T<T_C$ (b). 11

Figure 8– Polarization variations: Temperature and electric field dependent polarization variations of (a) BT, (b) PT, (c) 0.90PMN–0.10PT, and (d) 0.65PMN–0.35PT. 16

Figure 9– Pyroelectric behavior: Pyroelectric coefficient, p, of (a) BT, (b) PT, (c) 0.90PMN–0.10PT, and (d) 0.65PMN–0.35PT as a function of temperature and applied electric field E. 17

Figure 10– Heat capacity variations: Excess heat capacity of (a) BT, (b) PT, (c) 0.90PMN–0.10PT, and (d) 0.65PMN–0.35PT as a function of temperature and applied electric field E. 18

Figure 11– Adiabatic temperature changes: EC adiabatic temperature change, ΔT_{ad}, of (a) BT, (b) PT, (c) 0.90PMN–0.10PT, and (d) 0.65PMN–0.35PT as a function of temperature for ΔE ranging from 50 to 1000 kV/cm. The initial (biasing field) E_a is taken as 50 kV/cm. Also shown are experimentally measured EC data points (solid symbols) in BT, 0.90PMN–0.10PT, and 0.65PMN–0.35PT samples ([33, 60, 62]). 19

Figure 12– Adiabatic temperature change: Comparative adiabatic temperature change, ΔT_{ad}, of BT, PT, 0.90PMN–0.10PT, and 0.65PMN–0.35PT at different working temperatures: (a) ΔE=100 kV/cm and (b) ΔE=1000 kV/cm. The initial (biasing field) E_a is taken as 50 kV/cm. 20

Figure 13– Temperature Insensitivity: Comparative Full Width Half Maximum (FWHM) of the adiabatic temperature change of PT, BT, 0.90PMN–0.10PT, and 0.65PMN–0.35PT around their respective Curie temperatures. 21

Figure 14– Schematic of an elasto–electrocaloric refrigeration cycle: Application of electric field accompanied with mechanical tension on the material in an adiabatic system generates heat (1). This heat transfers to an external source (2) and upon removal of the stress, the material cools down (3). Removal of electric field and application of uniaxial compression further drops the temperature (4) resulting in heat transfer between the system and surroundings (5). This completes the cycle by taking the state of the system back to the initial stage (6). 29

Figure 15– Electrical and mechanical boundary conditions considered in this study: (a) uniaxial tension applied to a FE which results in an elastocaloric response; (b) a combination of hydrostatic pressure and an electric field acting on a single-domain ferroelectric material resulting in a combined elasto-electrocaloric response. 31

Figure 16– Elastocaloric response in BT: (a) polarization variations of BT under various applied uniaxial tensile fields (σ=100–500MPa) and (c) temperatures (T=RT–200°C) resulting in adiabatic temperature changes with values as high as ΔT_{ad}=1.8°C under σ=500 MPa (b) and ΔT_{ad}=1.72°C under σ=500 MPa at T=150 °C (d). 33

Figure 17– Elastocalotic response of different FE systems: adiabatic temperature change of PT (a) and (b), 0.90PMN–0.10PT (c) and (d), and 0.65PMN–0.35PT (e) and (f) as functions of temperature and applied tensile stress. PT exhibits the highest response at T=484°C at σ=500 MPa with a value of ΔT_{ad}=1.72°C. PMN–PT compositions display high values of ΔT_{ad} over a wider temperature range and closer to RT. 36

Figure 18– Electrocaloric response under hydrostatic pressure: adiabatic temperature change of BT (a), PT (b), 0.90PMN–0.10P (c), and 0.65PMN–0.35PT (d) as a function of temperature under various magnitudes of hydrostatic pressure. In all cases, hydrostatic pressure shifts the maxima to lower temperatures. This takes place at the cost of decreasing of the magnitude of the maximum value. Electric field is set to be $\Delta E=E_b-E_a$=100 kV/cm with initial field of E_a=0 kV/cm. 38

Figure 19– Strain and strain gradient variations: Effective strain throughout film thickness for (a) ultrathin film with thickness smaller than critical thickness for formation of misfit dislocations ($h<h_c$), (b) mediate film thicknesses and (c) relatively higher thiicknesses where the film fully relaxes after a certain point. (c), (d), and (f) presents the strain gradient throughout the film with thicknesses described in (a), (b), and (c)..... 47

Figure 20– Strain variations: (a) Effective misfit strain throughout film thickness and (b) strain gradient as a function of film thickness at various compressive misfit strains. h_c=5 nm is the Matthews–Blakeslee critical film thickness for formation of misfit dislocations. (c) shows the effective misfit strain and (d) shows strain gradient as a function of compressive misfit strain at various film thickness. Thicker films possess smaller effective misfit strain and strain gradients. Higher misfit stains imposes higher strain gradient and effective misfit strain..... 49

Figure 21– Strain profile of BT/ST system: Strain variation of epitaxial BT on ST substrate with misfit strain of u^0_m =-2.23% at film thicknesses of (a) 5, (b) 10, and (c) 20 nm. As the thickness increases both strain at the film substrate interface and strain gradient decrease..... 50

Figure 22– Adiabatic temperature change and misfit strain: (a) Contour plot of adiabatic temperature change at various temperatures and different misfit strains, and (b) adiabatic

temperature change variations as a function of temperature at different misfit strains for a 20 nm thick BT. A maximum of ΔT=1.81 °C is calculated at u^0_m =-2.5% at T=310 °C. As increases, the magnitude of the ΔT_{max} increases and the temperature at which it occurs shifts to higher temperatures. The inset in (b) exhibits the polarization variations as u^0_m changes. 54

Figure 23– Adiabatic temperature change and film thickness: (a) Contour plot of adiabatic temperature change at various temperatures and different film thicknesses, and (b) adiabatic temperature change variations as a function of temperature at different film thicknesses for a BT on ST substrate with u_m^0 =-2.23%. Maximum values of ΔT occurs at higher temperature and thinner films. As the film thickness increases, the magnitude of the ΔT_{max} decreases and the temperature at which it occurs shifts to lower temperatures. The inset in (b) exhibits the polarization variations as film thickness changes. 55

LIST OF TABLES

Table 1– Property coefficients: Property coefficients of BT, PT, 0.90PMN–0.10PT, and 0.65PMN–0.35PT. The data are compiled from Refs. [25, 49]..... 24

CHAPTER 1: INTRODUCTION

Solid–State Caloric Effect

In the past decade, there has been huge interest in the area of caloric effects in ferroelectrics (FE). In this effect, an external stimulus is the driving force for a reversible thermal change (adiabatic change in the temperature or isothermal change in the entropy) in the FE material [1]. Some of these caloric effects are electrocaloric (EC), mechanocaloric (mC), and flexocaloric (FC) effects [2–5]. This great deal of attention towards caloric effects is partly due to the quest for finding an alternative cooling system for current vapor–cycle cooling technologies which are poor in energy efficiency and have damaging environmental impact [6].

Moreover, multiple stimuli acting simultaneously or in a concerted sequence, could potentially yield to more pronounced caloric responses compared to the case where caloric effect is induced by any of the types of the stimuli individually [7]. This is why there also has been specific interest in searching for multicaloric material systems in recent years [8–13]. There are reports that suggest that multicaloric materials could enhance refrigerant efficiency and caloric responses [5, 8–10]. Also, values for coefficient of performance (COP) (defined as the ratio between the extracted heat with respect to the input work) as high as over 50% of Carnot efficiency can be achieved [14]. Therefore, it is crucially important to understand physics of this phenomena and optimize the caloric response. In order to do so, there are several aspects that need to be addressed (Figure 1)). The phenomenon should not change after repetitive cycles (reversibility). The temperature and entropy changes should be maximized. The temperature span of applicability should be broadened to fit into desirable working temperatures. The required filed strength should be minimized to avoid extra energy consumption and also prevent danger. Hysteresis losses should

be minimized. There should be control over fatigue to prevent material from failure. And finally, cost and environmental issues and always big concerns that need to be addressed.

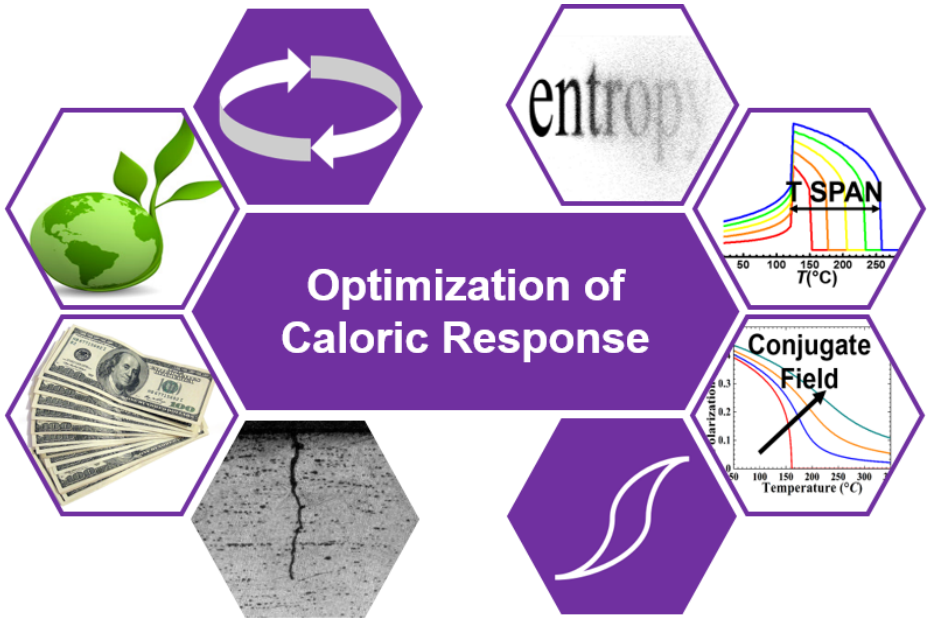

Figure 1– Various aspects of optimization of caloric responces in ferroelectric material systems: They include: reversibility, temperature and entropy changes, temperature span of applicability, filed strengths, hysteresis losses, cost and environmental concerns

In this thesis we discuss EC, mC, and FC effects in various FE material systems individually. We investigate the degree of which each of these effects can contribute in the overall caloric response of the selected material systems. We consider various factors such as geometry, temperature and also type and strength of the applied field. In the case of EC effect, application or removal of an electric field results in an adiabatic reversible temperature change (ΔT_{ad}) in an insulating polarizable material [15]. EC effect takes advantage of polarization and depolarization of FEs. It offers high operational temperatures and good tunability [16]. As for the case of mC effect, an applied stress field along the polar axis reversibly changes the temperature. Depending on the type of stress, one could name it elastocaloric (σC) or barocaloric effect [17]. As such, FC

effect is a result of flexoelectricity which is coupling between polarization and strain gradients [18]. There are reports that suggest that FC effect could have meaningful contributions to a multi−faceted caloric capacity of FE materials [16]. Similar to many of the physical properties in FEs, caloric effects are more pronounced in the vicinity of the structural phase transition.

Depending on the type of this transition the behavior of the material system varies. First−order phase transition exhibits a stronger caloric response. But at the same time, it has some shortcomings. The peak in temperature−ΔT_{ad} diagram is very sharp in temperatures near the transition temperature (T_C). Although values as high as 18 °C are achievable, the first−order phase transition often dictates a relatively narrow temperature range for high ΔT_{ad} values. In the second−order phase transitions, the peak is relatively broad. Besides, in most materials, hysteresis losses associated with regions close to first−order phase transition are detrimental [19, 20]. This results in low refrigerant efficiencies. On the other hand, there is no hysteresis losses related to second−order transition [21].

FE materials are emerging as a major choice to be considered for caloric systems [22, 23]. FEs benefit from the fact that there exist particular ways to improve their caloric responses. On one hand, one can make use of combination of positive and negative caloric responses [24], and manipulating the system by means such as mechanical stresses [25]. On the other hand, multiple giant caloric effects can coexist in FE material systems and contribute constructively. Hence, multicaloric materials could exhibit ΔT_{ad} values that exceed that of EC, mC, and other contributions alone [13].

Ferroelectricity

Non–centrosymmetry in the crystal lattice of a polarizable dielectric may give rise to emergence of a dipole moment in the absence of external fields. This dipole moment is called spontaneous polarization (P_S). This switchable polarization is the basic characteristic of FEs and its emergence is accompanied by a structural phase transition. This transition is always from a high–symmetry and high–temperature paraelectric (PE) phase to a lower–symmetry and low–temperature FE phase (Figure 2)) [26]. It usually causes strong anomalies in the behavior of physical properties such as dielectric, elastic, and thermal coefficients [27]. Also, there is a spontaneous strain associated with the PE–FE phase transition which is related to P_S via electro–strictive coefficients [28].

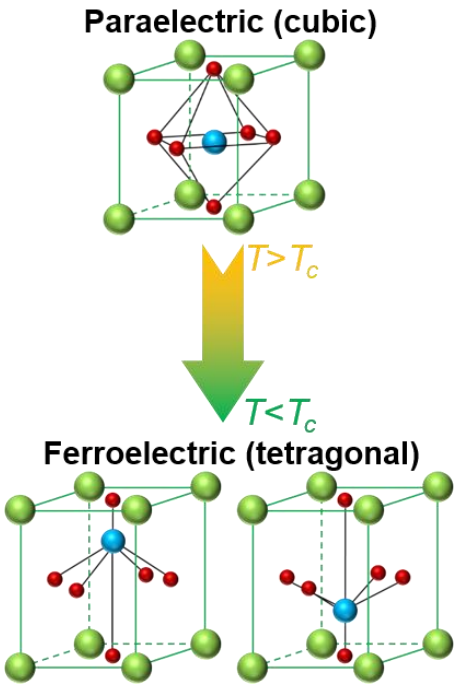

Figure 2– Structural paraelectric–ferroelectric phase transition: The structure changes from a centrosymmetrical cubic paraelectric phase to a non–centrosymmetrical tetragonal ferroelectric phase. The illustrated phases are perovskite structures where green, blue, and red spheres are anions, cations, and oxygen ions, respectively.

The temperature at which the PE–FE phase transition happens is called the Curie point, T_C. In the vicinity of T_C, as the temperature increases, the magnitude of dielectric permittivity (ε) increases and then abruptly decays above T_C. This can be observed from the Curie–Weiss law as [26]:

$$\varepsilon = \varepsilon_0 + \frac{C}{T - T_0} \approx \frac{C}{T - T_0} \tag{1}$$

In the Equation (1), C and T_0 are the Curie constant and Curie–Weiss temperature, respectively. Also, the change in the P_S vector with temperature T defines the pyroelectric effect which basically is the electrocaloric susceptibility:

$$p_i(T, E) = \left(\frac{\partial P_i^0}{\partial T} \right)_E = \left(\frac{\partial S}{\partial E} \right)_T \tag{2}$$

Where p_i ($Cm^{-2}K^{-1}$) is the vector of pyroelectric coefficients and S is the entropy [26]. Following from Equation ((2), examining the behavior of the excess entropy provides the way to examine how much the magnitude of the caloric effect varies subject to a change in electric field at constant temperature. The application of the external field which is conjugate to the order parameter P destroys the FE phase transition (Figure 3). Sufficiently large fields, will lead to disappearance of the discontinuities at the temperature T_C where the PE and FE phases are in equilibrium. Figure 3 presents the temperature variation of the polarization and dielectric permittivity near the first–order cubic to tetragonal FE phase transition for a BT crystal in the unconstrained and stress free (bulk) monodomain state as a function of various applied fields.

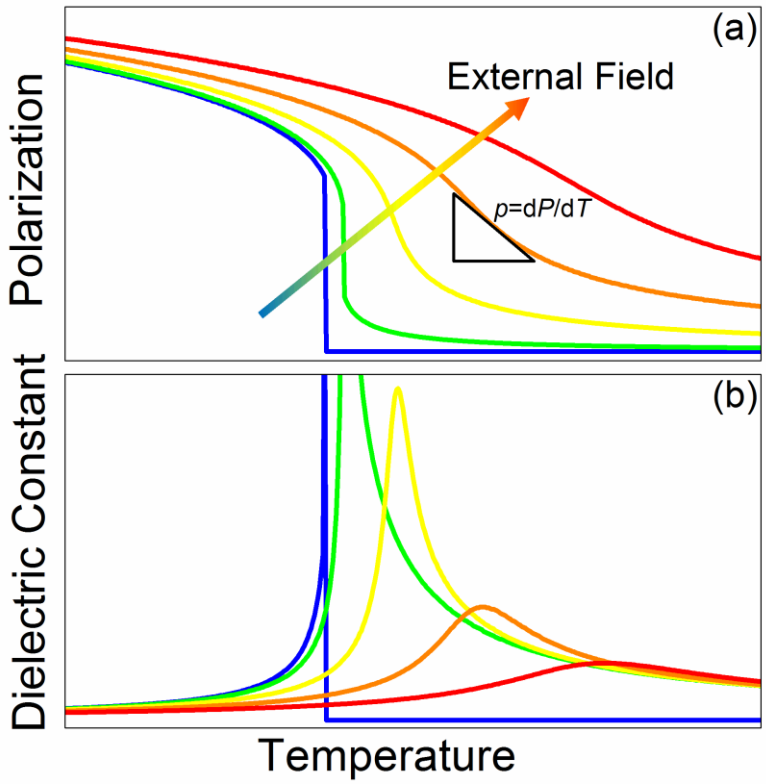

Figure 3– Change of (a) polarization and (b) dielectric constant of stress–free monodomain uniaxial barium titanate with temperature at various electric fields

In a configuration in which the FE material is sandwiched in between two electrodes, if the electrodes are located on the two major faces perpendicular to the polar axis, as illustrated in Figure 4(a), and the temperature changed at a rate dT/dt, then the short–circuit pyroelectric current would be:

$$i_p = Ap(T)\left(\frac{dT}{dt}\right) \tag{3}$$

The EC effect essentially is the converse of the pyroelectric effect (see Figure 4(b)). Here, an electric field applied to a polar dielectric causes a change in temperature in the material. The entropy and corresponding temperature changes are due to the relative movement of the ions in the structure under the applied field, and hence changes in order.

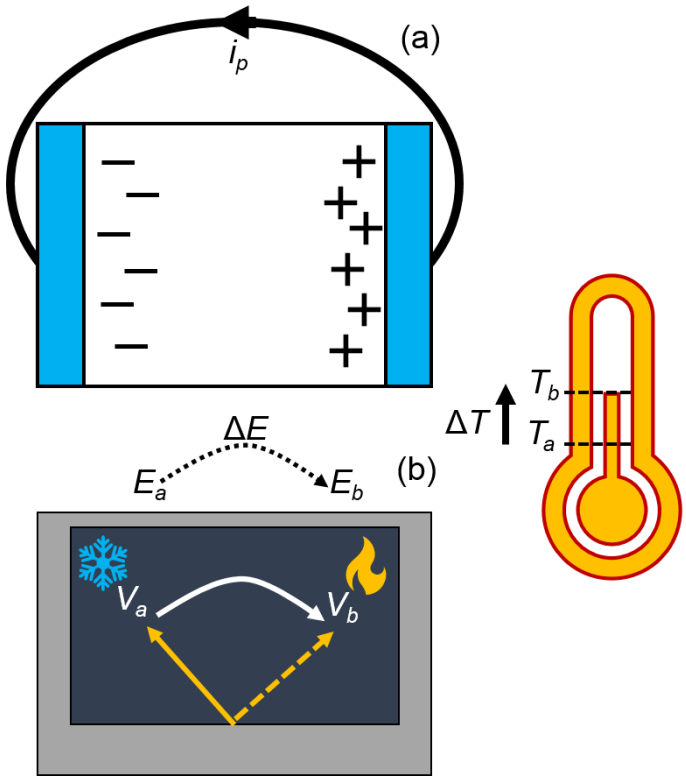

Figure 4– (a) Pyroelectric effect: a change in the temperature results in a variation in the polarization that generates a pyroelectric current; (c) Electrocaloric effect: A change in the applied electric field from E_a to E_b generates an electric field change ΔE that results in an adiabatic temperature variation ΔT_{ad}.

Coupling Between Mechanical, Electrical, and Thermal Properties in FEs

In FEs, external electric field induces electric charge through:

$$P_i = \chi_{ij} E_j \tag{4}$$

where χ_{ij} (Fm^{-1}) is the dielectric susceptibility. This electrical charge takes part in the dielectric displacement D_i via:

$$D_i = \varepsilon_0 E_i + P_i \tag{5}$$

where ε_0 is the dielectric permittivity of vacuum. The electric charge can also be induced by stress (X_{jk}) and/or temperature change (ΔT) through the piezoelectric and pyroelectric effects, respectively. These effects can be expressed as:

$$D_i = d_{ijk} X_{jk} \tag{6}$$

$$D_i = p_i \Delta T \tag{7}$$

in which, d_{ijk} and p_i are the piezoelectric and pyroelectric coefficients, respectively. Also, mechanical strains can be realized by induction of electric field, external stress, and temperature change, through the converse piezoelectric effect (Equation (8)), Hooke's law (Equation(9)), and thermal expansion, respectively.

$$x_{ij} = d_{kij} E_k \tag{8}$$

$$x_{ij} = s_{ijkl} X_{kl} \tag{9}$$

In Equations (8) and (9), x_{ij} is the strain and s_{ijkl} are the elastic compliance coefficients. Similarly, entropy changes can occur as a result of temperature change, external mechanical fields, and external electric field through heat capacity, mC effect, and EC effect, respectively. In FE materials, an external stimulus can promote, suppress, or even reverse spontaneous polarization. As a matter of fact, caloric effects in FEs are a direct consequence of how this switchable polarization behaves under various fields. Caloric effect is often huge near their structural FE–PE phase transition [21]. This is due to the fact that, total entropy of a FE system changes significantly in the vicinity of FE–PE transition. Therefore, in the light of this concept, applied driving fields such as electrical and mechanical fields can contributes to emergence of changes in thermal behavior of the material (Figure 5) [29].

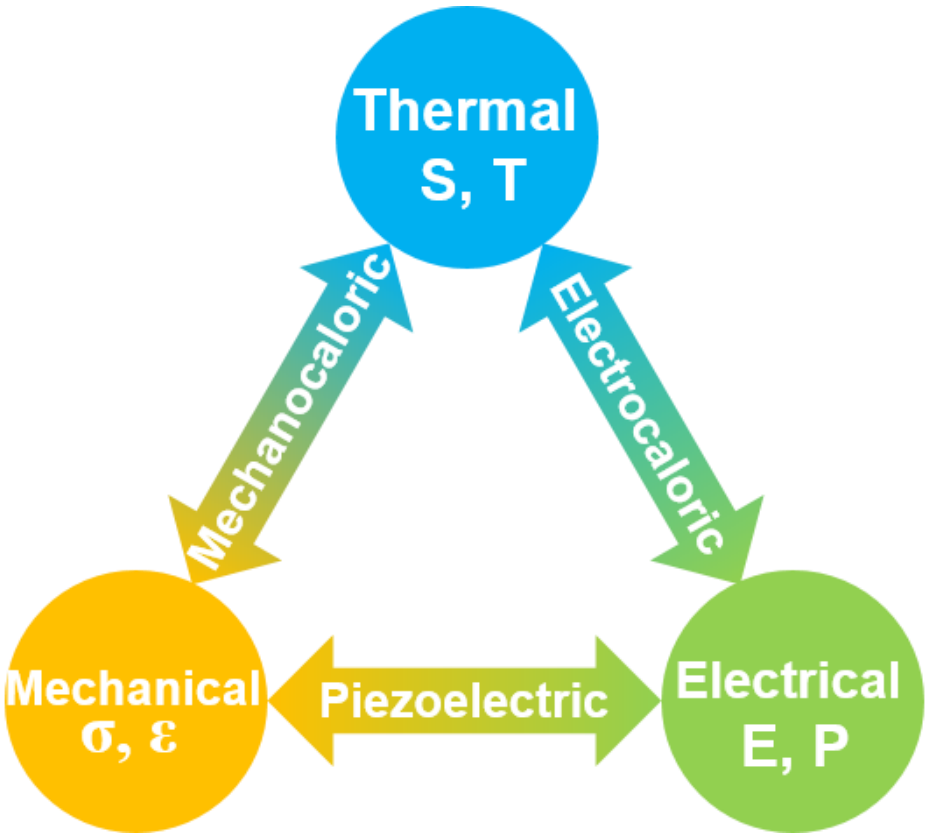

Figure 5– Coupling between mechanical, electrical, and thermal properties in FEs

Thermodynamic Formulation

We use a well–established thermodynamic approach to study the coupling between thermal, mechanical, and electrical parameters of selected FE material systems [30]. We then derive the equations of state to investigate physical properties. Slight changes in the electric displacement d*D*, strain d*x*, and entropy d*S* results in a reversible change in the internal energy *U*:

$$dU = TdS + X_{ij}dx_{ij} + E_i dD_i \tag{10}$$

Performing a Legendre transformation, we switch to Gibbs free energy ($G = U - TS - X_{ij}x_{ij} - E_i D_i$) and change the independent variables from (*S*, *x*, *D*) to (*T*, *X*, *E*). Hence [26]:

$$dG = -SdT - x_{ij}dX_{ij} - D_i dE_i \tag{11}$$

$$S = -\left(\frac{\partial G}{\partial T}\right)_{X,E} \rightarrow dS = \left(\frac{\partial S}{\partial T}\right)_{X,E} dT + \left(\frac{\partial S}{\partial X_{ij}}\right)_{T,E} dX_{ij} + \left(\frac{\partial S}{\partial E_i}\right)_{T,X} dE_i \tag{12}$$

$$x_{ij} = -\left(\frac{\partial G}{\partial X_{ij}}\right)_{T,E} \rightarrow dx_{ij} = \left(\frac{\partial x_{ij}}{\partial T}\right)_{X,E} dT + \left(\frac{\partial x_{ij}}{\partial X_{kl}}\right)_{T,E} dX_{ij} + \left(\frac{\partial x_{ij}}{\partial E_k}\right)_{T,X} dE_k \tag{13}$$

$$D_i = -\left(\frac{\partial G}{\partial E_i}\right)_{T,X} \rightarrow dx_{ij} = \left(\frac{\partial D_i}{\partial T}\right)_{X,E} dT + \left(\frac{\partial D_i}{\partial X_{jk}}\right)_{T,E} dX_{ij} + \left(\frac{\partial D_i}{\partial E_j}\right)_{T,X} dE_j \tag{14}$$

Using Equations (12–14), we can determine various direct and coupling physical effects from partial derivatives as depicted in Figure 6.

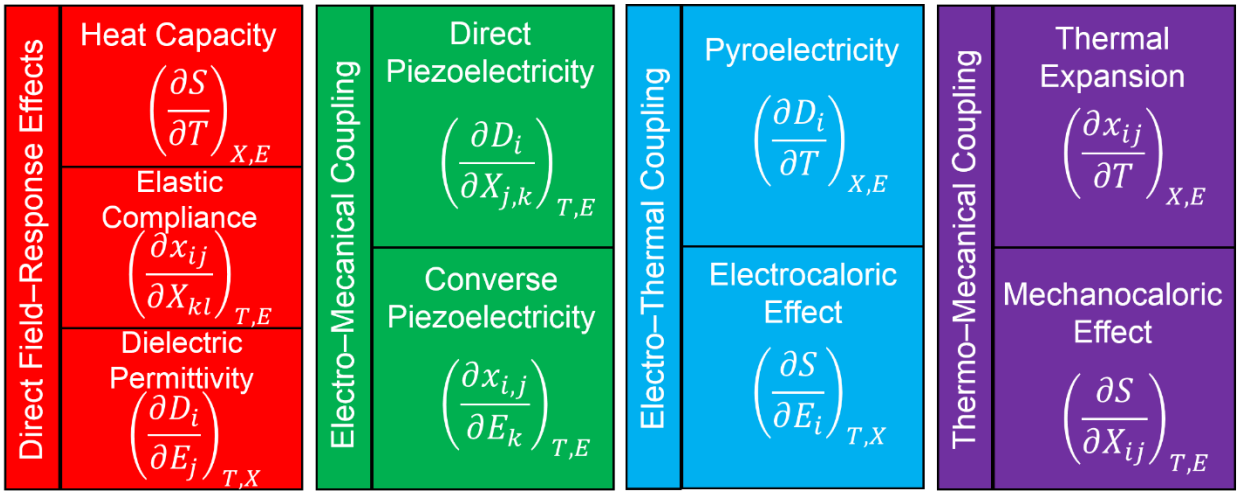

Figure 6– Direct and coupling physical effects and corresponding thermodynamic relations

The main focus of this thesis is on electro–thermal (EC effect) and thermo–mechanical (σC and barocaloric effects) couplings in selected FE material systems.

Thermodynamics of Ferroelectrics

The PE–FE phase transition may be either of a first or a second order. Behavior of the partial derivative of the Gibbs free energy (G) with respect to temperature (T) defines the order of the phase transition. In a first–order phase transition, the first derivative of G with respect to T is discontinuous at T_C in the absence of an external field. As for the second–order phase transition, the second derivative of G with respect to T is discontinuous in the absence of an external field. Barium titanate (Figure 7) as a FE is an example of a first–order phase transition. Application of a sufficiently large external field could wash out the first–order phase transition (see Figure 7(a)).

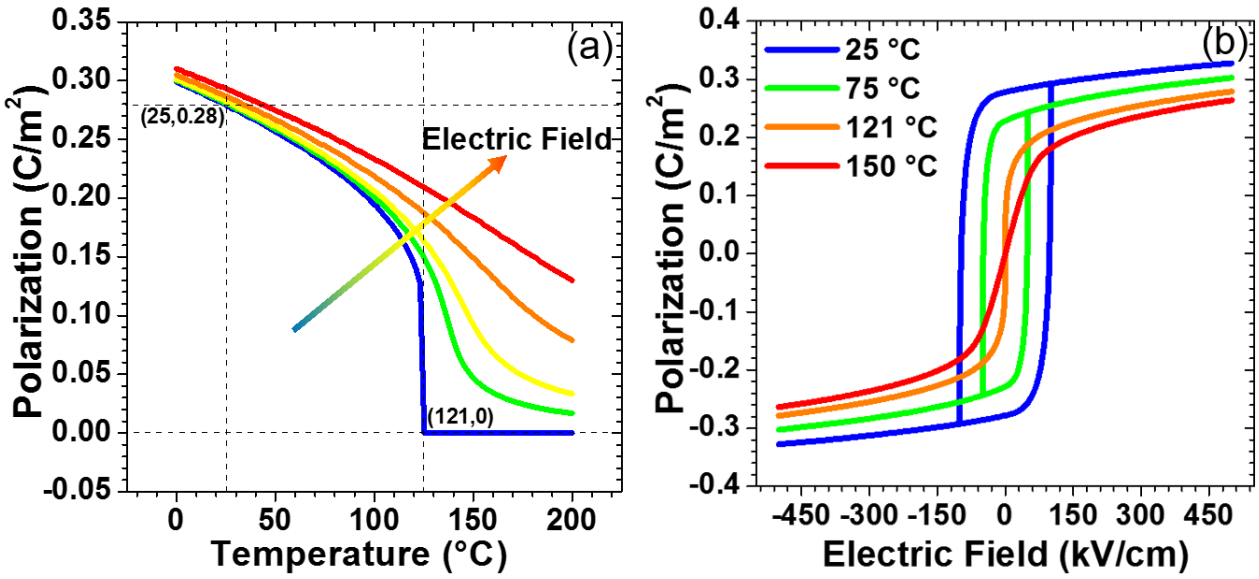

Figure 7– Polarization variations of barium titanate as functions of temperature and electric field: First order phase transition smears as the electric field is applied (a) and a ferroelectric hysteresis loop starts to shape up once the temperature decreases to $T<T_C$ (b).

Besides first–order phase transitions, x·Pb($Mg_{1/3}Nb_{2/3}$)O_3–(1-x)·$PbTiO_3$ [xPMN–(1-x)PT] (PMN–PT) solid solutions as relaxor–FEs is an example of a second–order like phase transitions. Dielectric permittivity (ε) in these relaxor–FEs display broad maximums which is a strong function

of frequency at temperatures below their highest ε ($T_{\varepsilon(\max)}$). Above $T_{\varepsilon(\max)}$ however, relaxor–FEs do not follow the Curie–Weiss behavior.

Objectives of the Thesis

We apply a generalized thermodynamic theory of caloric effects with a phenomenological approach to various FE material systems. This generalized theory allows us to analytically study different types of caloric effects that display various types of cross–couplings. In particular, we take cases for EC, mC (σC and barocaloric), and FC effects and evaluate the magnitude of caloric responses in every case for four different classes of materials. They include weak first–order phase transition barium titanate (BT), strong first–order phase transition lead titanate (PT), and two compositions of second–order PMN–PT one far away from the morphotropic phase boundary (MPB) (PMN–10PT) and one close to the MPB (PMN–35PT). In the case of EC and mC effects, we determine intrinsic entropy and temperature changes in mentioned perovskite FEs using theoretical tools supported by experimentally measured heat capacities as a function of the applied electric field and temperature. We provide a quantitative analysis of the thermal, pyroelectric, EC, and mC properties of representative ceramic FE systems. Moreover, the FC response of selected FE material systems are computed due to generation of strain gradient induced via misfit dislocations. Considering the electromechanical coupling between the polarization and stress gradient, a nonlinear thermodynamic model is employed that takes into account the appropriate mechanical boundary conditions. These misfit dislocations result in strong strain variations through the film thickness in epitaxially grown barium titanate. Overall, this work aims to implement modeling tools that are capable of predicting caloric effects in FE materials. This will be beneficial to future developments in the area of solid–state cooling/heating technologies.

CHAPTER 2: CALORIC EFFECTS IN FERROELECTRICS

Electrocaloric Effect

Since the first observance nearly a decade ago of a giant EC effect in thin film FE $PbZr_{0.95}Ti_{0.05}O_3$ by Mischenko *et al.* [31], the field of FE based solid state electrothermal interconversion has seen rapid advancement, significantly improving both the magnitude of usable EC temperature change ΔT_{ad}, and the available cooling capacity as defined by an enthalpy (ΔH) or entropy (ΔS) variation: $\Delta H = \Delta S \cdot \Delta T_{ad}$ [32–35]. Several materials systems have been proposed for use in electrothermal applications including FE/anti–FE ceramics in their single–crystal, bulk, and thin film forms, FE polymers/co–polymers/terpolymers, and liquid crystals [3, 36–42]. These efforts have primarily been led through experimentation, augmented by expert intuition [24]. The success of such an approach is demonstrated by the more than fourfold improvement in ΔT_{ad} with a concomitant increase in ΔH of similar magnitude [34]. Fundamental enhancements in material properties of this kind directly impact system level performance and costs, reducing the effects of parasitic losses and potentially yielding system level performance competitive with vapor compression systems [37].

Many applications of FEs, from random memory (FRAMs) devices [43], to piezoelectric actuators [25, 44], and pyroelectric infrared detectors [45], have all benefitted (and often been directed) by multi–scale theoretical approaches including *ab initio* and beyond first principles methods [46, 47], non–linear thermodynamics, and atomistic models [48–50]. Thus, it is compelling to employ similar methods as a means for understanding the material properties and discovering new materials systems for ECs. We present here a complete analysis of intrinsic adiabatic temperature changes in perovskite FEs using theoretical tools supported by carefully measured heat capacities [51] as a function of the applied electric field and temperature.

Specifically, thermal, pyroelectric and EC properties of prototypical FEs BT, PT, and relaxor–FEs PMN–PT compounds are computed. Two specific compositions of PMN–PT were chosen as representatives of a relaxor and a relaxor–FE solid solution, 0.90PMN–0.10PT and 0.65PMN–0.35PT, respectively. 0.90PMN–0.10PT is a relaxor composition that is far from the MPB. 0.65PMN–0.35PT lies in close proximity of the MPB, where pseudo–rhombohedral, pseudo–monoclinic/orthorhombic, and pseudo–tetragonal phases can co–exist and phase transitions can be induced through applied electric and elastic fields [52]. This system is of particular interest because it displays a strong order–disorder and crystallographic phase transitions which couple with external stimuli. These particular characteristics are arguably at the core of the very large electromechanical response exhibited by PMN–PT (with or without additional doping) which are used in high–strain actuators/transducers [53]. The very large electromechanical response has been attributed to the inherently (intrinsic) large piezoelectric response that stems from ionic displacements [54], a large "extrinsic" contribution from highly adaptive nano– and mesoscale domain structures [55], and a strong contribution from electrostriction [56]. A relatively large temperature change of ~5 ^{o}C at an applied field difference of ~900 kV/cm and T=75 ^{o}C has been reported for this solid solution for 90PMN–10PT [52].

Our analysis is based on the methodology that is described in detail in the section of "Materials and Methods". It uncovers two significant findings. Firstly, the *intrinsic* adiabatic temperature changes in relaxor–FEs are substantial and relatively temperature insensitive. ΔT_{ad}s as high as 14°C can be achieved with applied fields on the order of 1 MV/cm at T~350 °C for (001) oriented 0.65PMN–0.35PT. This EC response does not vary over a large temperature interval: ΔT_{ad}=13±1°C for 200<T<600°C. Secondly, our studies indicate that one can find perovskite FEs with exceedingly large *intrinsic* EC effects. ΔT_{ad} is ~28°C in PT for an applied field of 1 MV/cm,

rivaling the best EC response observed in polymer FEs [57, 58]. This is particularly important since only limited fundamental studies of the EC response exist in perovskite systems at high fields [59, 60].

Polarization, Heat Capacity, and Pyroelectric Coefficient

In Figure 8, we plot the equilibrium (spontaneous) polarization P^0 as functions of T and applied electric field E for PT, BT, 0.90PMN–0.10PT, and 0.65PMN–0.35PT. As expected, BT and PT display first–order phase transitions as described by the jump in P^0 for E=0 at the FE–PE transformation temperature T_C.

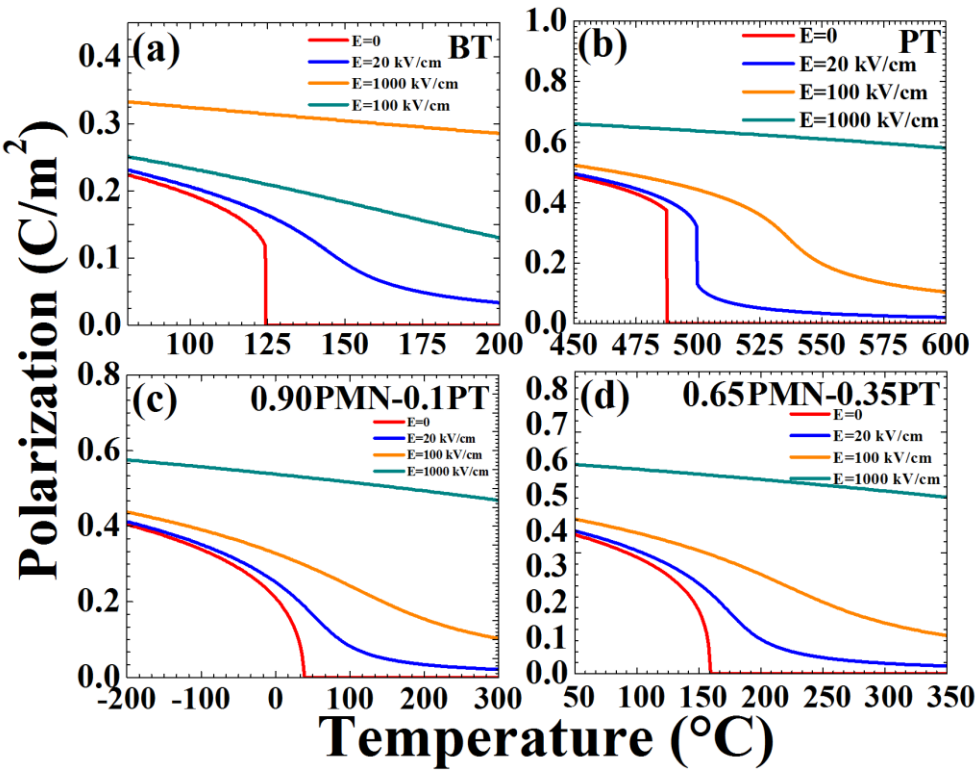

Figure 8– Polarization variations: Temperature and electric field dependent polarization variations of (a) BT, (b) PT, (c) 0.90PMN–0.10PT, and (d) 0.65PMN–0.35PT.

In BT, this first–order phase transition is weaker compared to PT as characterized by the magnitude of the polarization jump at the respective T_Cs. An applied electric field in the direction

of the spontaneous polarization "smears" the phase transformation and it destroys the discontinuities in thermodynamic properties that are a function of polarization at the phase transition temperature. For BT, a field as high as 20 kV/cm is sufficient to smear out the first–order phase transition where as in PT, higher fields are required (E=100 kV/cm). On the other hand, both PMN–PT compositions display a second–order phase transitions. Here, there is no discontinuity at T_C in the polarization response and the effect of the applied electric field is similar resulting in a smearing of the phase transformation.

In Figure 9 and Figure 10 we plot the temperature dependence of the p and the $C^{XS}{}_E$ for the four materials investigated for E = 0, 20, 100, and 1000 kV/cm. These parameters are defined through the Maxwell equations as described in the section of "Materials and Methods'" and are essentially partial derivatives of the polarization with respect to temperature.

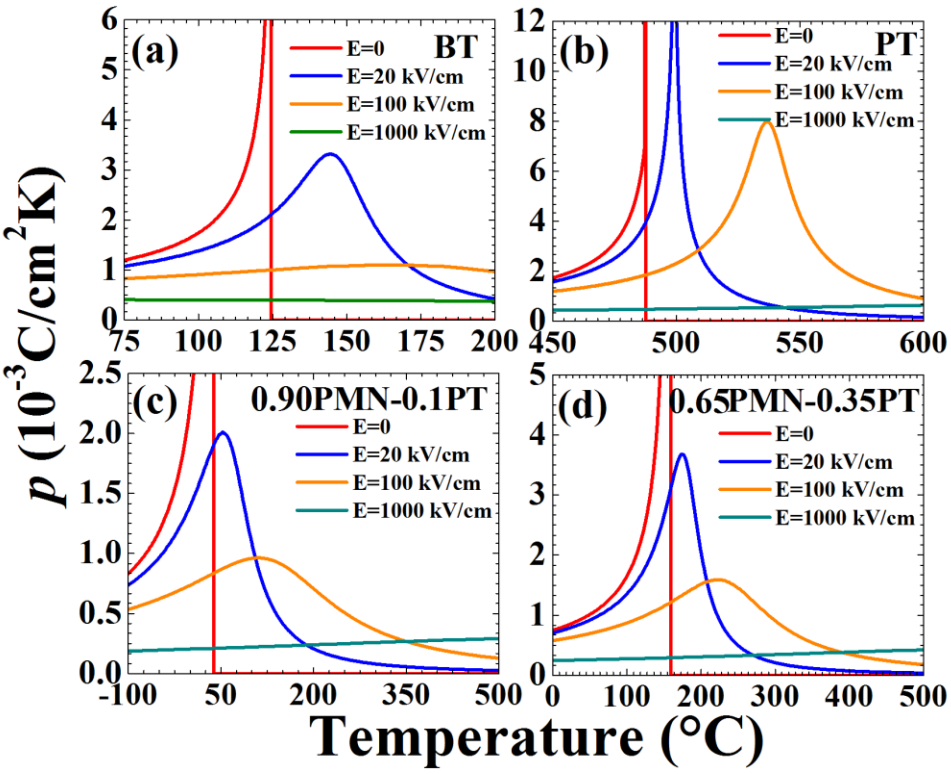

Figure 9– Pyroelectric behavior: Pyroelectric coefficient, p, of (a) BT, (b) PT, (c) 0.90PMN–0.10PT, and (d) 0.65PMN–0.35PT as a function of temperature and applied electric field E.

As such, near T_C, these quantities display a λ–type anomaly and this anomaly disappears with the application of an electric field in the direction of the equilibrium polarization. The behavior shown in Figures 8–10 are expected responses and the relevant thermodynamic background can be found elsewhere [61].

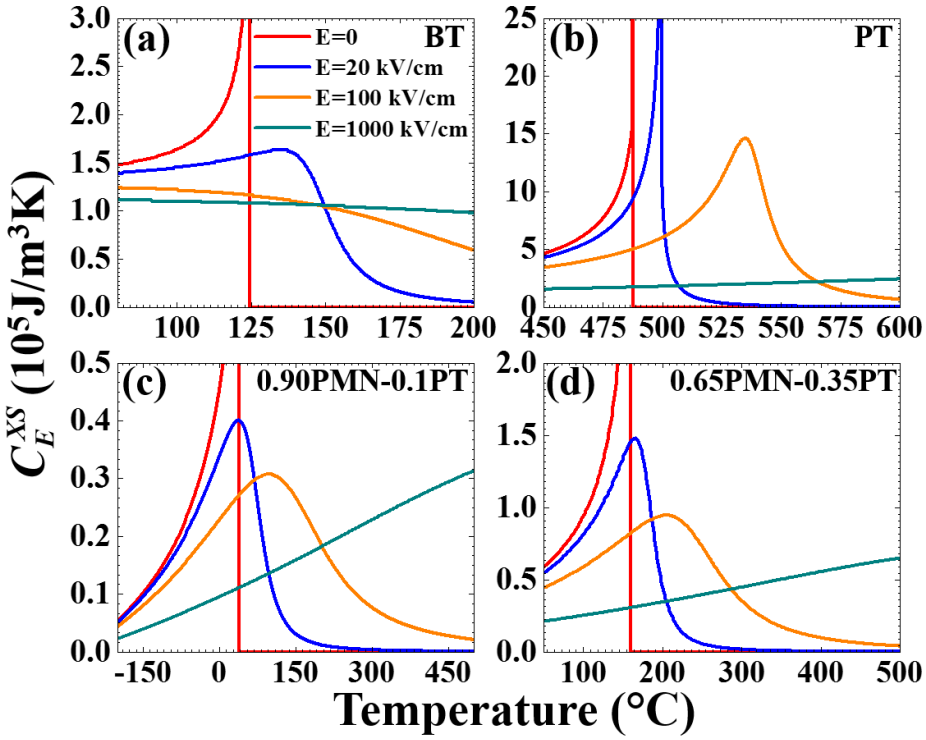

Figure 10– Heat capacity variations: Excess heat capacity of (a) BT, (b) PT, (c) 0.90PMN–0.10PT, and (d) 0.65PMN–0.35PT as a function of temperature and applied electric field *E*.

Adiabatic Temperature Change

It is necessary to experimentally determine or to be able to compute the reversible adiabatic temperature variation (ΔT_{ad}) near and away from the FE–PE phase transformation temperature (T_C) as this is a critical parameter in the estimation of the system–level coefficients of performance. The temperature dependence of ΔT_{ad} as functions of T and ΔE are thus plotted in Figure 11.

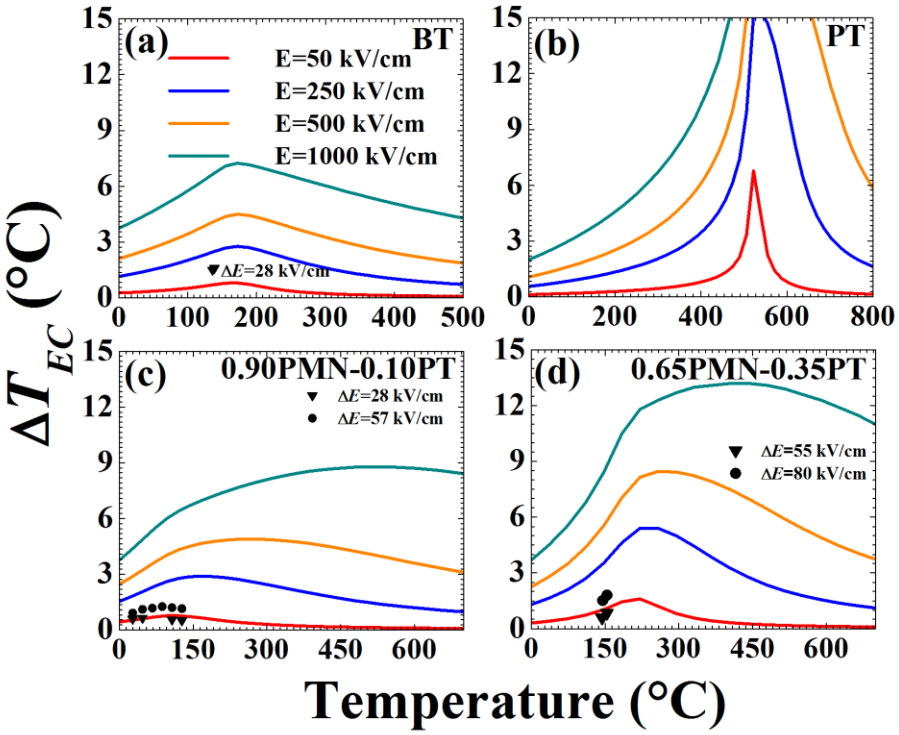

Figure 11– Adiabatic temperature changes: EC adiabatic temperature change, ΔT_{ad}, of (a) BT, (b) PT, (c) 0.90PMN–0.10PT, and (d) 0.65PMN–0.35PT as a function of temperature for ΔE ranging from 50 to 1000 kV/cm. The initial (biasing field) E_a is taken as 50 kV/cm. Also shown are experimentally measured EC data points (solid symbols) in BT, 0.90PMN–0.10PT, and 0.65PMN–0.35PT samples ([33, 60, 62]).

For BT and two PMN–PT systems we found agreement with directly measured EC data at lower fields (solid symbols). In all cases, the field change ΔE is taken relative to an initial bias of E_a=50 kV/cm. For BT near T_C (121 °C), ΔT_{ad} is found to be 0.8, 2.8, 4.4, and 7.3 °C for ΔE=50, 250, 500, and 1000 kV/cm. For PT, the EC response near T_C = 490 °C is significantly larger, where ΔT_{ad} =3.2, 15.0, 21.1, and 28.5 °C for these same field levels. We attribute the larger response to the substantially more pronounced first–order phase transformation in PT compared to BT, as discussed in detail by Zhang *et al.* [63].

For both 0.90PMN–0.10PT and 0.90PMN–0.35PT, the ΔT_{ad} responses are much broader and relatively less temperature sensitive as shown in Figure 11(c) and (d), respectively, compared to BT and PT. In the case of 0.90PMN–0.10PT, ΔT_{ad}=0.8, 2.9, 4.9, and 8.8 °C for ΔE=50, 250,

500, 1000 kV/cm, respectively, near its T_C of 38 °C. For 0.65PMN–0.35PT (T_C=159 °C), the EC response is considerably larger; ΔT_{ad}=1.6, 5.5, 8.5, and 13.1 °C for ΔE=50, 250, 500, 1000 kV/cm, respectively.

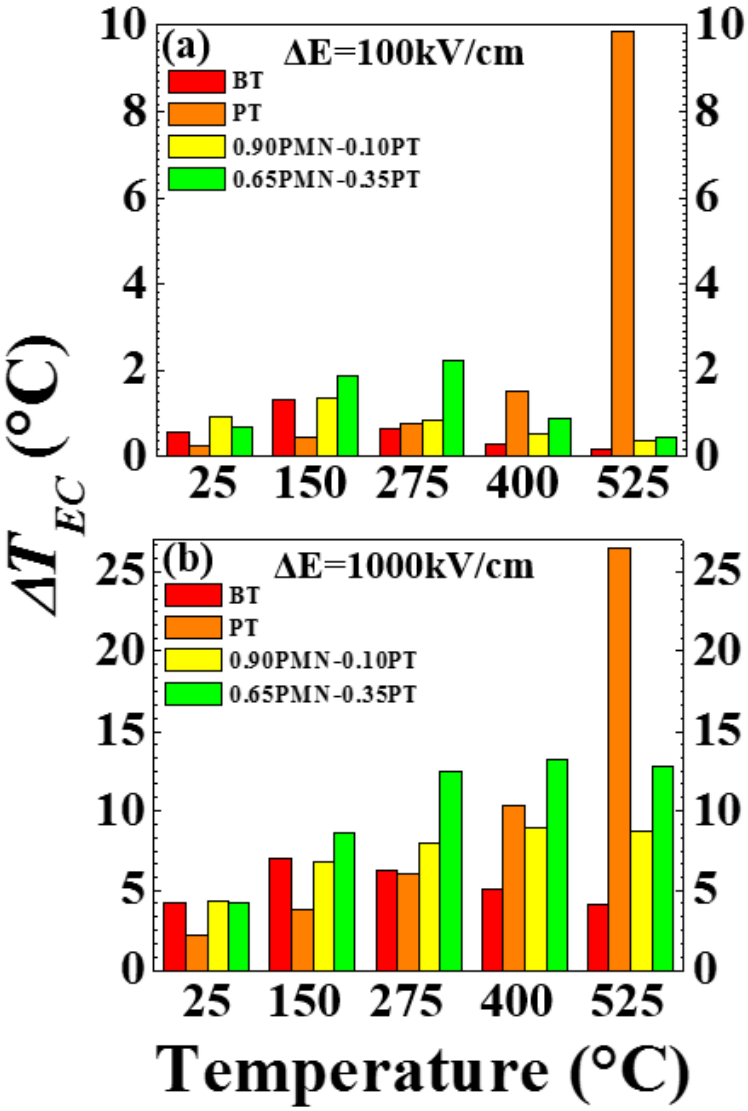

Figure 12– Adiabatic temperature change: Comparative adiabatic temperature change, ΔT_{ad}, of BT, PT, 0.90PMN–0.10PT, and 0.65PMN–0.35PT at different working temperatures: (a) ΔE=100 kV/cm and (b) ΔE=1000 kV/cm. The initial (biasing field) E_a is taken as 50 kV/cm.

We show in Figure 12 a more detailed comparison of the EC response of all four materials in at four specific temperatures of 25, 150, 175, 400 and 525 °C, at an intermediate field of ΔE=100 kV/cm (Figure 12(a)) and a relatively higher field of ΔE=1000 kV/cm (Figure 12(b)). In both

cases, E_a was taken to be 50 kV/cm. In order to provide a quantitative illustration of the temperature sensitivity of the EC adiabatic temperature change as a function of the applied field, we plot the full width half maximum (FWHM) of ΔT_{ad} for all four materials studied herein.

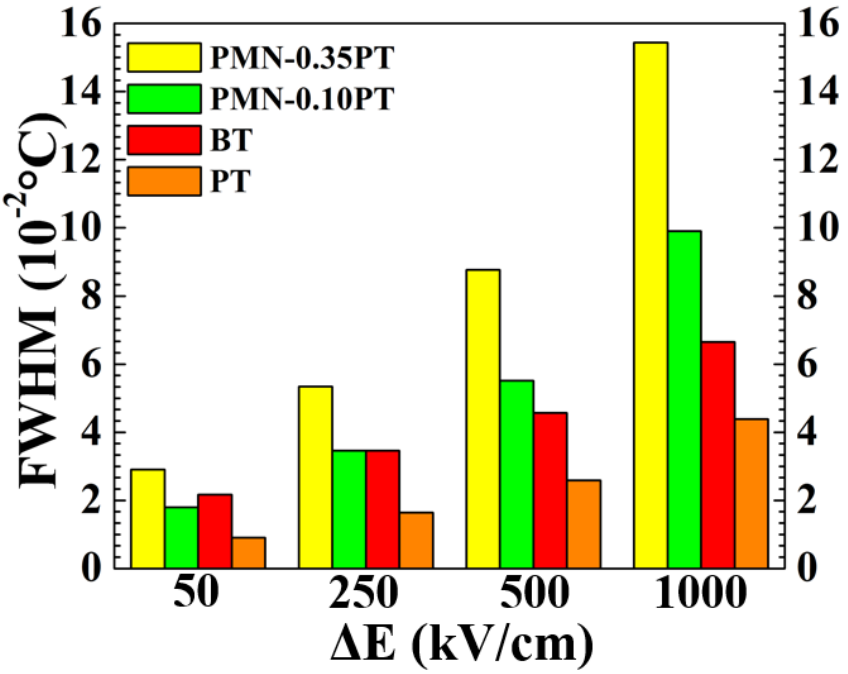

Figure 13– Temperature Insensitivity: Comparative Full Width Half Maximum (FWHM) of the adiabatic temperature change of PT, BT, 0.90PMN–0.10PT, and 0.65PMN–0.35PT around their respective Curie temperatures.

Figure 13 shows FWHM of these materials at four different field variations corresponding to ΔE=50, 250, 500, and 1000 kV/cm and E_a=50 kV/cm.

Analyzing the Electrocaloric Effect

For E=0, there is a λ–anomaly associated with the first–order FE to PE phase transformation, resulting in (theoretically) an infinitely large p and ${C^{XS}}_E$ at the equilibrium transition temperature T_C. The application of high enough E along the polarization direction results in the smearing of the temperature dependence of p and ${C^{XS}}_E$ as shown in Figure 9 and 10 for all four materials. This results in the disappearance of well–defined maxima in these properties at

sufficiently large electric fields: the maxima in p and $C^{XS}{}_E$ shift to higher temperatures and are reduced in magnitude with an increase in E. Furthermore, these quantities become progressively less sensitive to temperature for larger fields. In the case of PT, however, owing to a much stronger first–order FE–PE phase change as defined by the jump in the spontaneous polarization at T_C (see Figure 8), relatively higher electric fields are required to achieve the same effect. At lower field difference, all four materials show typical FE behavior such that there is an increase in the value ΔT_{ad} with operating temperature, up to a point around their respective T_C. There is a decrease in ΔT_{ad} beyond a maximum near the T_C with increasing temperature which is expected [63] since the pyroelectric response for $T>T_C$ for small electric fields is essentially given by the variation of the electric field induced polarization in the PE phase. For significantly higher fields, the EC response of PT and BT shows a maximum in ΔT_{ad} near T_C and a decrease for $T>T_C$. However, in the cases of 0.90PMN–0.10PT and 0.65PMN–0.35PT, ΔE=1000 kV/cm is sufficiently large to obscure the effect of the phase transition at T_C, at least for temperatures in which the material retains it FE properties. Such a difference in behavior can be assigned, at least in part, to the presence of a relaxor nature of the FE solid solutions, and the accompanying dispersion of the FE–PE transition [64]. Application of a large enough electric field can also be expected to result in a partial stabilization of the FE phase to slightly higher temperatures than T_C [65]. Also, as it can be seen in Figure 13), both 0.90PMN–0.10PT and 0.65PMN–0.35PT have a relatively temperature insensitive ΔT_{ad} over a larger temperature range compared to PT and BT.

The large peak in EC response of the PMN–PT composition corresponding to the MPB is similar to the previously calculated (and experimentally confirmed) peaks in the dielectric, piezoelectric and elastic compliance at the MPB for lead zirconate–lead titanate (PZT) solid solutions [66]. The enhancement in the properties are often attributed to the co–presence of two

(or more) phases with differing polarization directions [67]. This could be attributed to the disappearance of anisotropy contributions to the free energy and formation of nano–domains.

We note that the calculated values in this work are limited to intrinsic EC response. Effective functional responses in ferroic materials are due to both their intrinsic (lattice) and extrinsic nature which includes motion of domain walls, formation of phase boundaries, and local (defect) dipoles. While the amount of extrinsic contributions to the effective EC response has not been quantified, such data are indeed available for the dielectric response, and in part, also for the piezoelectric response of the materials considered here. In general, relaxor–FEs such as PMN–PT have been shown to exhibit enhanced extrinsic properties that can be as high as 30%–80% of the total functional response in BT and PZT ceramics [68]. This contribution could be significantly larger in Relaxor–$PbTiO_3$ near MPB single crystals, evaluated to be ~300% [69]. We can, therefore, expect that the overall EC response of these single crystals to be similarly augmented by the extrinsic contributions, and through domain wall engineering, i.e. creation of specific mobile (adaptive) domain architectures to further enhance entropy variations with an applied electric field. This enhancement should be more pronounced at relatively low initial biases.

Materials and Methods

Details of Theoretical Methodology

We consider a monodomain single crystal FE in an unconstrained, unstressed state. We analyze PT, BT, 0.90PMN–0.10PT, and 0.65PMN–0.35PT that undergo a cubic (Pm3m) PE to tetragonal (P4mm) FE transition at T_C. The components of the polarization vector **P** for the PE and the FE phases are $P_1=P_2=P_3=0$ and $P_1=P_2=0$, $P_3=P\neq0$, respectively. The volumetric (excess) free energy due to polarization is given by:

$$G(T,E,P) = G_0 + \alpha_1 P^2 + \alpha_{11} P^4 + \alpha_{111} P^6 - EP \quad (15)$$

where G_0 is the free energy density of the (unpolarized) PE phase, and α_1, α_{11}, and α_{111} are dielectric stiffness coefficients. α_1 is given by the Curie–Weiss law such that $\alpha_0=(T–T_C)/(2\varepsilon_0 C)^{-1}$ where ε_0 is the permittivity of space and C is the Curie–Weiss constant. In Equation (15), $\mathbf{E}=(0,0,E_3=E)$ is the applied electric field. All thermodynamic properties and stiffness coefficients used in the computations are given in Table 1).

Table 1– Property coefficients: Property coefficients of BT, PT, 0.90PMN–0.10PT, and 0.65PMN–0.35PT. The data are compiled from Refs. [25, 49]

Parameter/Material	BT	PT	0.90PMN–0.10PT	0.65PMN–0.35PT
T_C (°C)	121	475	38	159
α_1 (10^5m/F)	3.76($T–T_C$)	3.68($T–T_C$)	1.81($T–T_C$)	2.415 ($T–Tc$)
α_{11} (10^6m^5/C^{2}F)	3.6T–630	–146–0.38T	61.6–0.038T	28.9–0.038T
α_{111} (10^9m^8/C^{4}F)	6.6	0.257	0.257	0.257
S_{11} (10^{12}m^2/N)	8.3	7.7	0.018	0.31
S_{12} (10^{12}m^2/N)	–2.73	–2.33	–0.63	–0.11
S_{44} (10^{12}m^2/N)	9.22	8.77	–0.56	0.245
Q_{11} (m^4/C^2)	0.11	0.09	0.084	0.084
Q_{12} (m^4/C^2)	–0.034	–0.025	–0.025	–0.025
Q_{44} (m^4/C^2)	0.029	0.039	0.035	0.035
Hard Mode C_E (10^6J/gK)	3.74	4	$8(5\times10^{-9}\times T^3 – 3\times10^6\times T^2+6\times10^{-4}\times T+0.31)$	$8(4\times10^{-9}\times T^3-3\times10^{-6}\times T^2+8\times10^{-4}\times T+0.3)$

For PMN–PT, we use Heitmann–Rossetti free energy potentials that were obtained using a combined phenomenological and topological analysis [70]. The free energy potentials are supplemented by experimental ‘‘hard–mode’’ contributions to heat capacity determined experimentally (see description below and Ref. [61]). The equilibrium polarization P^0 is then determined via solving the equation of state $\partial G / \partial P = 0$.

The two most important factors in determining the adiabatic temperature change ΔT_{ad} at a given T with an applied electric field difference $\Delta E = (E_b\text{-}E_a)$ are: the pyroelectric coefficient of

the material, p, and the heat capacity at constant E, $C^{XS}{}_E$. The proper definitions of these quantities follow from the relevant Maxwell relations. At constant E, the excess entropy S_E^{XS}, the excess specific heat ΔC, and the pyroelectric coefficient p follow from:

$$S_E^{XS}(T,E) = -\left(\frac{\partial G^0}{\partial T}\right)_E, \tag{16}$$

$$\Delta C_E(T,E) = -T\left(\frac{\partial^2 G^0}{\partial T^2}\right)_E, \text{ and} \tag{17}$$

$$p(T,E) = \left(\frac{\partial^2 P^0}{\partial T}\right)_E = \left(\frac{\partial S}{\partial E}\right)_T \tag{18}$$

The adiabatic temperature change (ΔT_{ad}) as result of a change in the electric field strength $\Delta E = E_b - E_a$ can then be calculated via:

$$\Delta T_{EC}(T,E) = -T\int_{E_a}^{E_b} \frac{1}{C_E}\left(\frac{\partial P^0}{\partial T}\right)_E dE \tag{19}$$

For all materials studied in this investigation, we estimate the absolute value of specific heat, $C_E(T, E)$ by adding the computed zero–field values of the excess specific heat $\Delta C_E(T, E)$ from Equation (17) to the lattice or hard–mode contributions taken from the experimental values.

Experimental Details

A direct method for determining the EC effect is given in Refs. [32, 62, 71–73]. The (total) heat capacity at constant electric field E (C_E) was determined using either a high–resolution calorimeter described in Refs. [51, 71, 74] or a conventional Quantum Design Physical Properties Measurement System (PPMS) technique. Quantitative and qualitative agreement between the

calculated and measured data provided additional support for the robustness of our approach. For the direct EC measurements, a high–resolution calorimeter with small modifications to the experimental setup has been utilized to measure a sample temperature variation due to the EC when an external field was applied. A step voltage form is applied to all the samples by a high–voltage generator. The sample temperature was acquired by a small bead thermistor attached to the sample electrode. The surrounding bath temperature was stabilized by a temperature controller within 0.1 mK. In typical sequence the field was switched on to some level for 500 seconds and then switched off. During this time and additional 500 seconds after the switching off the field the relaxation of the sample's temperature was monitored. This allows detailed analysis of the amplitude of the EC temperature change induced by the electric field as described in details in Ref. [32].

Electrocaloric Effect: Summary

In summary, we have calculated the EC temperature changes in BT, PT, 0.90PMN–0.10PT, and 0.65PMN–0.35PT over a wide range of temperatures. Large EC responses close to or exceeding 10^{o}C were found over a very broad temperature range exceeding several hundred degrees in case of BT, and two PMN–PT systems. In PT, a giant EC response of 28 ^{o}C at 1MV/cm is predicted. These adiabatic temperature changes correspond to significant entropy variations. For example, ΔS=-22.16 and -7.29 $J \cdot kg^{-1} \cdot K^{-1}$ for PT and 0.65PMN–0.35PT, respectively for temperatures at which each material shows the maximum ΔT_{ad} (561 °C for PT and 253 °C for 0.65PMN–0.35PT). This is similar to some of the best EC responses experimentally observed at similar fields in polymeric FEs. $\Delta T_{ad}(\Delta E)$ shows little saturation at large fields indicating that in these materials truly very large EC response is achievable [22]. Therefore, it may prove optimal for application to operate these materials at large fields as demonstrated recently in thick films.

Mechanocaloric Effect

Definitions and Importance

Solid–state caloric materials have been receiving a great deal of attention in the past decade since the discovery of giant EC adiabatic temperature variations in thin films [31]. The goal is to utilize them as an alternative to conventional cooling systems [3, 5, 22, 42, 75]. Advances in understanding these types of materials could result in efficient means to realize solid–state power interconversion devices that produce high temperature lifts in smaller volumes. These devices can be utilized in a wide variety of applications such as localized cooling and refrigeration (i.e. food processing, biomedical, personal cooling), on–chip cooling, residential and commercial heating, ventilation and air conditioning systems, and temperature regulations of sensors [36]. In caloric materials, external stimuli result in isothermal entropy variations, which ultimately lead to adiabatic temperature changes (ΔT_{ad}). These stimuli include electric, magnetic or stress fields, and as a result, the material exhibits an EC [5, 15], a magneto–caloric (MC) [2, 76], or an σC effect [6, 11], respectively. Furthermore, in multi–ferroic systems, a combination of appropriate conjugate fields gives rise to a *multicaloric* response that is essentially the total adiabatic temperature variation due to all entropy changes.

When compared to MC and purely σC materials (ferromagnets and ferroelastics, respectively), FEs, which could utilize the combined EC and σC effects, offer a significantly easier means to apply an external stimulus (electric vs. magnetic fields) and do not suffer from mechanical fatigue as severely as shape memory alloys (SMAs) [77–79]. The interest in FEs stems from the fact that there are large entropy changes associated with the emergence of spontaneous polarization and spontaneous self–strain below the FE–PE phase transformation temperature (T_C) [80, 81]. There are several FE materials that have been studied for EC applications. Some examples

include FE and anti–FE ceramics, polymers and copolymers, and in bulk, single–crystal, and thin film forms [3, 15, 36–38, 82]. Furthermore, FE heterostructures consisting of FE and linear dielectrics have been shown to exhibit enhancements in ΔT_{ad} as a function of volume fraction of the FE material. This is due to strong electrostatic coupling between the linear dielectric and the FE [37, 80, 83]. A recent theoretical study suggests that the amplitudon and the phason modes of polarization can be decoupled in complex layered oxides, which may create two independent channels of entropy [84]. These correspond to the increase in the magnitude of the polarization vector (amplitudon) and its rotation (phason) upon the application of an external electric field. We note that there are also experimental issues in realizing the measurement of actual adiabatic temperature changes. There have been methods developed to measure this directly in addition to approaches that determine the adiabatic temperature changes from Maxwell equations by determining temperature variations of the polarization and the dielectric constant. There is an ongoing debate about the benefits on such measurements [85, 86]. As a final remark, we must also point out that intrinsically, the adiabatic temperature change resulting from entropy variations with applied electric field (i.e. the EC effect) is limited in its magnitude [85].

FE phase transformations in inorganic systems can be of first– or second–order and such phase transformations involve non–centrosymmetric displacements resulting in a spontaneous polarization and strain. Thus, the σC effect can also be realized in FEs such as prototypical BT and PT. For example, in PT, the self–strain associated with the cubic–tetragonal PE–FE phase transformation is 1.62% just below T_C = 475 ^{o}C and 4.87% at room temperature (RT=25 ^{o}C). This spontaneous strain is on the order of what has been observed in single crystal SMAs (~8% at RT in Ni–Ti alloys) [87, 88]. This is the reason why several studies in recent years have concentrated on maximizing the total caloric properties of FEs by combining EC *and* σC effects [6, 9, 24, 89,

90]. Experimental studies report moderate combined (total) ΔT_{ad} in bulk and thin film FEs. For example, FE $(Ba_{0.85}Ca_{0.15})(Zr_{0.1}Ti_{0.9})O_3$ ceramic exhibits an adiabatic temperature change of ΔT_{ad}=1.55°C at T=67°C, hydrostatic pressure of 250 MPa and applied electric field (E) of 20 kV/cm [9]. Relaxor xPMN–(1–x)PT with composition of 0.68PMN–0.32PT displays a total ΔT_{ad}=0.36°C at T=67°C, pressure of 28 MPa and E=15 kV/cm [8].

While these values of ΔT_{ad} are fairly modest, we note that the corresponding driving fields to obtain these variations are small. Therefore, ΔT_{ad} should be substantially larger for a *combination* of relatively large electric fields and mechanical stresses. We present a systematic theoretical analysis of intrinsic EC and σC properties of different FE and relaxor–FE materials that could be used in a hypothetical refrigeration cycle shown in Figure 14.

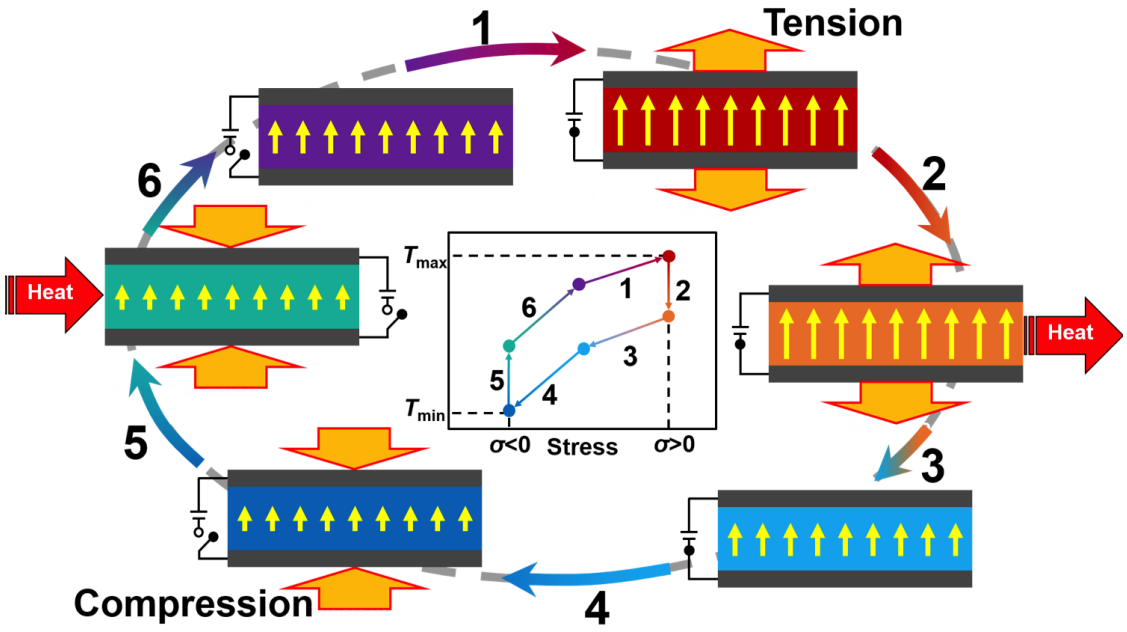

Figure 14– Schematic of an elasto–electrocaloric refrigeration cycle: Application of electric field accompanied with mechanical tension on the material in an adiabatic system generates heat (1). This heat transfers to an external source (2) and upon removal of the stress, the material cools down (3). Removal of electric field and application of uniaxial compression further drops the temperature (4) resulting in heat transfer between the system and surroundings (5). This completes the cycle by taking the state of the system back to the initial stage (6).

In this illustration, a combination of electric fields [38] and uniaxial stresses [24] are employed to generate entropy changes, which lead to heat exchange with the system environment. An adiabatic increase in the tensile stress is accompanied by the application of an electric field, and thus, increases the temperature of the system. This results in a heat transfer between the system and its surroundings. Upon the gradual removal of the stress field, the temperature drops. There is an additional decrease in the temperature with the application of a compressive stress and the removal of an electric field. This is followed by absorbing heat from the external source. At this step, removal of compressive field again increases the temperature. This completes the cycle by taking the system to its initial state. Specifically, we compute the combined intrinsic EC–σC behavior of prototypical FEs BT and PT, and relaxor–FE PMN–PT solid solutions. We choose two specific compositions for PMN–PT: 0.90PMN–0.10PT and 0.65PMN–0.35PT. These represent a relaxor and relaxor–FE solid solution, respectively. 0.90PMN–0.10PT is far from the MPB with a maximum dielectric response at around 40°C. The maximum ΔT_{ad} shifts to higher temperatures upon the application of an electric field [15]. 0.65PMN–0.35PT is near the MPB and displays promising caloric responses [91]. It is noteworthy that large pyroelectric coefficient values (1070 $\mu Cm^{-2}°C^{-1}$) have been observed in 0.72PMN–0.28PT and 0.67PMN–0.33PT [92]. The selection of these four systems also allows us to compare caloric behavior of relaxor PMN–PT with prototypical FEs BT and PT.

Theoretical Approach

In order to analyze EC–σC properties of FE perovskites we employ a Landau–Devonshire approach. We consider a monodomain single–crystal FE with tetragonal symmetry (P4mm). The FE is cubic (Pm3m) in its unpolarized PE state. The FE is sandwiched between two metallic electrodes and there is a (external) uniaxial tensile stress that acts on the system along the axis of

spontaneous polarization [see Figure 15(a)]. The excess free energy due to polarization in the FE state is:

$$G(T,P,\sigma,E) = G_0 + (\alpha_1 - Q_{11}\sigma)P^2 + \alpha_{11}P^4 + \alpha_{111}P^6 + \alpha_{1111}P^8 - EP - \frac{1}{2}S_{11}\sigma^2 \qquad (20)$$

where G_0 is the free energy density of the PE state and P is the polarization in the FE state, i.e., the polarization vector $\mathbf{P}=(P_1, P_2, P_3)=(0, 0, P)$. E and σ are the components of applied electric field and uniaxial stress, respectively, and both are oriented parallel to the polarization direction P. α_1, α_{11}, α_{111}, and α_{1111} are the dielectric stiffness coefficients. Q_{11} is the electrostrictive coefficient and S_{11} is the elastic compliance. α_1 obeys the Curie–Weiss law such that $\alpha_1 = (T–T_C) / (2\varepsilon_0 C)$ where ε_0 is the permittivity of space and C is the Curie–Weiss constant.

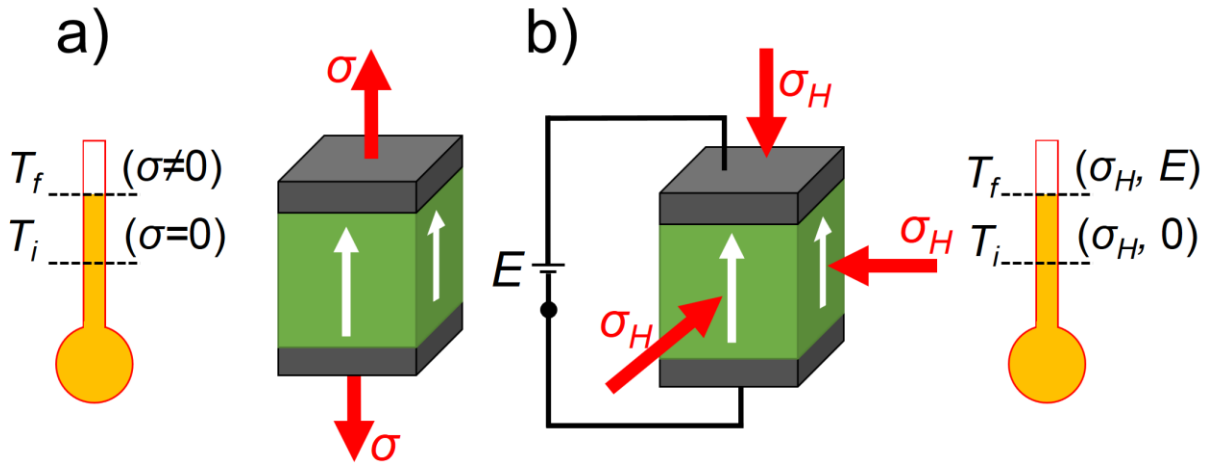

Figure 15– Electrical and mechanical boundary conditions considered in this study: (a) uniaxial tension applied to a FE which results in an elastocaloric response; (b) a combination of hydrostatic pressure and an electric field acting on a single-domain ferroelectric material resulting in a combined elasto-electrocaloric response.

In order to calculate the ΔT_{ad} due to external stimuli, we use a formulation proposed by Pirc *et al.*, [93] which stipulates that the entropy of a FE system under an external field ϕ can be written as a sum of polarization dependent dipolar entropy (S_{dip}) and lattice entropy (S_{latt}):

$$S(\phi,T) = S_{dip}(\phi,T) + S_{latt}(T) \tag{21}$$

S_{dip} is a strong function of external electric and/or stress fields since the equilibrium polarization of the system changes with the application of these quantities. Variations in S_{latt} with ϕ are negligible [93]. In our approach, the system starts off at an initial state (ϕ_1, T_1) and the cycle closes at a final state (ϕ_2, T_2). The entropy variation of the system is zero. This leads to:

$$\Delta S = \left[S_{dip}(\phi_2,T_2) + S_{latt}(T_2)\right] - \left[S_{dip}(\phi_1,T_1) + S_{latt}(T_1)\right] = 0 \tag{22}$$

and thus, the change in lattice entropy is obtained with:

$$S_{latt}(T_2) - S_{latt}(T_1) = \int_{T_1}^{T_2} \frac{C_{latt}(T)}{T} dT \cong C_{latt}(T_1) \ln\left(\frac{T_2}{T_1}\right) \tag{23}$$

where C_{latt} is the (volumetric) lattice heat capacity and its absolute value is estimated by scaling the zero–field values of specific heat of the PE–FE transition to the hard–mode contributions to the specific heat taken from experimental data [94]. Via solving Equation (23) for T_2 gives a self–consistent equation for $\Delta T_{ad} = T_2 - T_1$:

$$T_2 = T_1 \exp\left[-\frac{1}{C_{latt}}\left[S_{dip}(\phi_2,T_2) - S_{dip}(\phi_1,T_1)\right]\right] \tag{24}$$

where $S_{dip} = -T\cdot(\partial(\Delta G)/\partial T)_{\phi}$. Considering that only α_1 and α_{11} are temperature dependent, Equation (24) becomes:

$$T_2 = T_1 \exp\left[\frac{1}{2C_{latt}}\left[\frac{d\alpha_1}{dT}\left(P^2(\phi_2,T_2)-P^2(\phi_1,T_1)\right)+\frac{d\alpha_{11}}{dT}\left(P^2(\phi_2,T_2)-P^2(\phi_1,T_1)\right)\right]\right] \quad (25)$$

This is the key relation that allows us to compute and compare ΔT_{ad} for the four different FEs. The relevant coefficients entered in Equations (20–25) are compiled from available literature and are listed in Table 1). Also included in this table are the hard modes of C_{latt} as a function of temperature.

Elastocaloric Response

Figure 16 presents the σC behavior [obtained from Equations (20–25) for E=0] of BT as functions of temperature and tensile stress fields, which stabilize the tetragonal FE phase by shifting the transition temperature T_C towards higher temperatures.

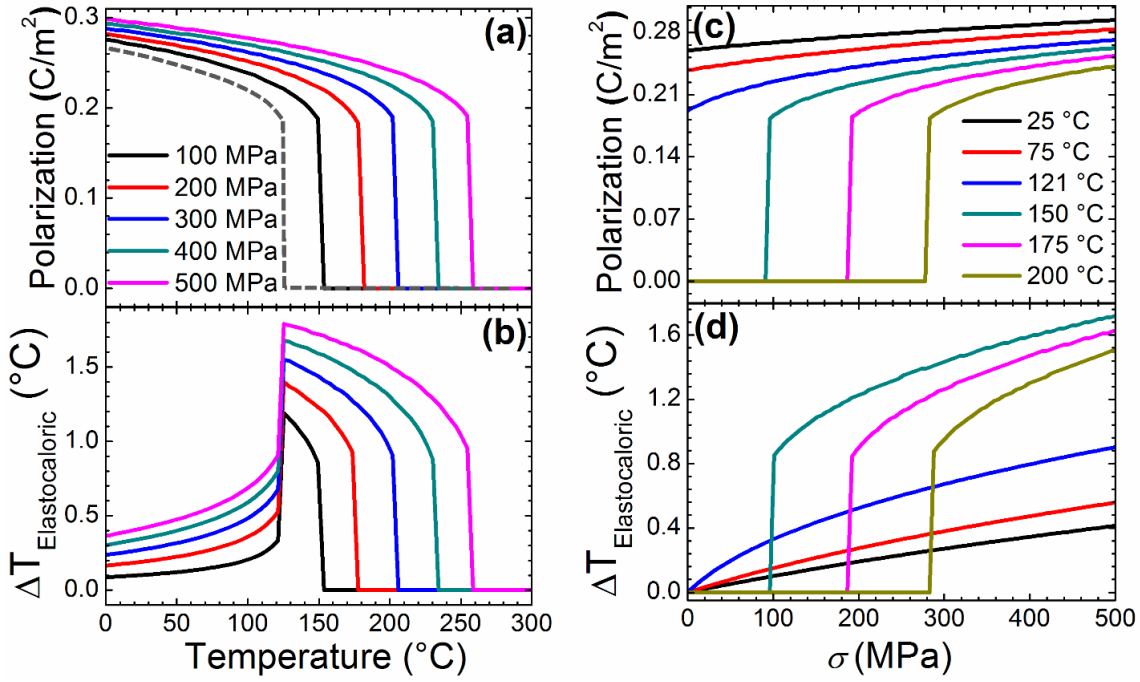

Figure 16– Elastocaloric response in BT: (a) polarization variations of BT under various applied uniaxial tensile fields (σ=100–500MPa) and (c) temperatures (T=RT–200°C) resulting in adiabatic temperature changes with values as high as ΔT_{ad}=1.8°C under σ=500 MPa (b) and ΔT_{ad}=1.72°C under σ=500 MPa at T=150 °C (d).

The application of σ to values as high as 500 MPa can shift T_C by as much as 140°C. ΔT_{ad} associated with the applied tensile stress is shown in Figure 16(b). Stronger tensile stress fields lead to higher values of maximum ΔT_{ad}; for σ=100, 200, 300, 400 and 500 MPa, $\Delta T_{ad,max}$=1.2, 1.4, 1.6, 1.7, and 1.8°C, respectively. This happens at $T = T_C$ (σ=0) =125°C in all cases because the initial (bias) stress is zero. Depending on the strength of the stress field, the temperature range at which noticeable values of ΔT_{ad} are observed varies. Comparing Figure 16(a) and (b), it is evident that both the polarization and ΔT_{ad} abruptly drop at the same temperature. The shift in the Curie point as a function of applied stress is given by:

$$\Delta T_C = T_{C(\sigma \neq 0)} - T_{C(\sigma=0)} = 2\varepsilon_0 C Q_{11} \sigma \tag{26}$$

which can be obtained by setting α_1-$Q_{11}\sigma$ to zero [see Equation (20) and the definition of the α_1]. Here $T_C(\sigma=0)$ is the bulk, unstrained Curie transition temperature. Figure 16(a) shows the variation in T_C as a function of σ. As expected, higher tensile stresses stabilize the FE phase. We note that the transition is still of first–order since the material is not clamped [95, 96], i.e., unlike α_1, α_{11} in Equation (20) is not normalized with respect to σ. What is surprising is that the maximum of ΔT_{ad} is not near this new transition point. It is still around the bulk T_C. The reason for this is that the initial stress for the compositions of ΔT_{ad} is σ=0. This ensures that the maximum ΔT_{ad} is near $T_{C(\sigma=0)}$. The magnitude of the applied stress then determines the broadness of the ΔT_{ad} curve. For example, at σ=100 MPa this range is around 20°C whereas for σ=500, it increases to a span of ~135°C.

Another way of showing the correlation between T and σ is by analyzing how polarization changes as a function of σ at a given T. This is illustrated in Figure 16(c) which shows that an external tensile stress in the direction of the easy polarization axis of BT increases the value of

polarization at a given T. For $T < T_{C(\sigma\neq0)}$, there is a gradual, continuous increase in the equilibrium polarization. However, for temperatures higher than $T_{C(\sigma\neq0)}$, an abrupt shift takes place at different magnitudes of σ. This is due to the stress–induced FE phase transformation. For example, for BT at 200^{o}C, an applied uniaxial tensile stress of 280 MPa will favor a FE state. The jump of 0.18 Cm^{-2} at 200^{o}C and 280 MPa is an indication of a strong first–order phase transition. This response is reflected in the ΔT_{ad} behavior, which is shown in Figure16(d). Tensile stresses in the FE state [$T < T_{C(\sigma\neq0)}$] result in a continuous, but small increase in σC properties. A more significant variation in ΔT_{ad} can be expected if $T > T_{C(\sigma\neq0)}$ where the stress induced FE transformation results in more extensive entropy variations. We note that the correlations between P_S, T and σ are reversed for compressive stresses (σ<0) since these would suppress FE behavior and shift T_C to temperatures lower than the unconstrained, unstressed T_C of BT. It is worth mentioning that the values of ΔT_{ad} calculated here are in the same range as EC adiabatic temperature change of BT that are reported in experimental studies [62, 97]. This indicates how combined σC and EC effects can enhance the cooling potential of such material systems.

In Figure (17), we present σC behavior of PT, 0.90PMN–0.10PT, and 0.65PMN–0.35PT using the methodology developed for BT. We plot ΔT_{ad} as a function of temperature at various stress fields as well as ΔT_{ad} as a function of σ at different temperatures. Similar to BT, PT has a strong first–order phase transition.

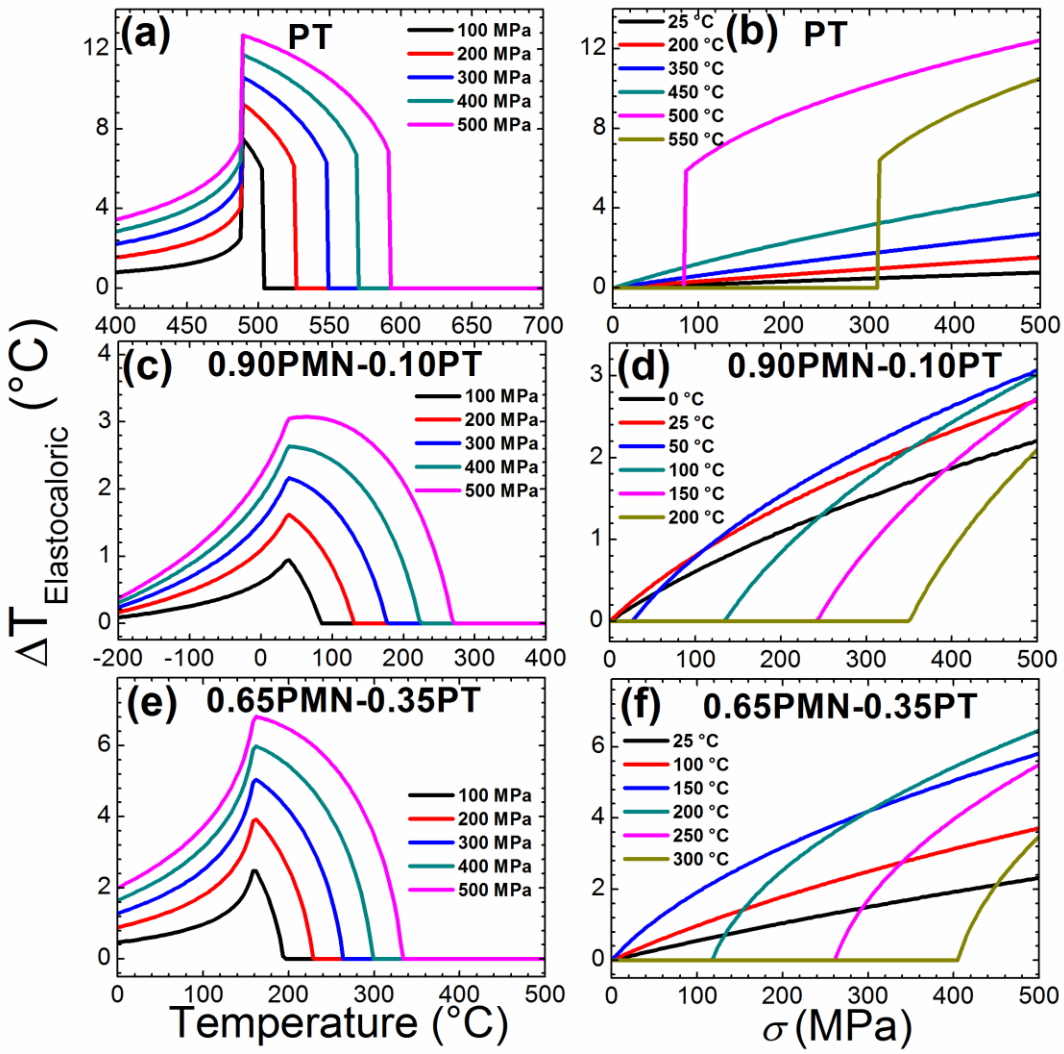

Figure 17– Elastocalotic response of different FE systems: adiabatic temperature change of PT (a) and (b), 0.90PMN–0.10PT (c) and (d), and 0.65PMN–0.35PT (e) and (f) as functions of temperature and applied tensile stress. PT exhibits the highest response at T=484°C at σ=500 MPa with a value of ΔT_{ad}=1.72°C. PMN–PT compositions display high values of ΔT_{ad} over a wider temperature range and closer to RT.

This results in sharp peaks in Figure 17(a) with large drops following the disappearance of polarization beyond $T > T_{C(\sigma\neq0)}$. ΔT_{ad} can reach as much as 12.7 °C upon the application of σ=500 MPa. For lower stress levels such as σ=100, 200, 300, and 400 MPa, ΔT_{ad} = 7.5, 9.3, 10.6, and 11.7°C, respectively. The temperature range with relatively high values of ΔT_{ad} shows a similar behavior and expands with increasing σ. It goes from 14°C to 37, 60, 81, and 103 °C for σ=100,

200, 300, 400, and 500 MPa, respectively. The values of ΔT_{ad} for PT are higher when compared to BT under similar conditions. This is because PT has a stronger first–order phase transformation than BT: generating a more substantial variation in entropy as PT transforms from an unpolarized PE to the FE state. It is important to mention that maximum values of ΔT_{ad} for PT occur at higher working temperatures compared to BT.

In the case of PMN–PT, the second–order phase transition produces slight changes in the overall appearance of ΔT_{ad} as functions of T and σ. In both compositions of PMN–PT chosen for this study, the ΔT_{ad} responses are much broader and relatively less temperature sensitive compared to BT and PT [Figures 16(b) and 17(a), respectively]. For 0.90PMN–0.10PT, the values of $\Delta T_{ad,\max}$ change from ~1.0 to 3.1°C as σ increases from 100 to 500 MPa. As for the temperature range with relatively high ΔT_{ad}, the relaxor nature of FE phase transformation results in the widening of the temperature range for ΔT_{ad}. For instance, values of $\Delta T_{ad} > 1$°C are achievable for a temperature range of $-105^{o}\text{C} < T < 243^{o}\text{C}$ at σ=500 MPa. Figure17(e) shows a similar behavior for 0.65PMN–0.35PT, but with a more pronounced manner. For 0.65PMN–0.35PT, $\Delta T_{ad,\max}$=2.5, 4.0, 5.0, 6.0, and 6.8°C for σ=100, 200, 300, 400, and 500 MPa, respectively. Moreover, for stress fields as low as σ=200 MPa, $\Delta T_{ad} > 1$°C is achievable for a temperature range as wide as $21^{o}\text{C} < T < 218$°C.

Stress Mediated Electrocaloric Response (Hydrostatic Pressure)

As for the application of stress, the most facile approach is with hydrostatic pressure since it allows for higher magnitudes of stresses in ceramics. The combined effect of hydrostatic pressure and an applied electric field is explored using a similar approach [Figure 15(b)]. The free energy in this case is:

$$G_H = G_0 + (\alpha_1 - 2Q_{11}\sigma_H + 2Q_{12}\sigma_H)P^2 + \alpha_{11}P^4 + \alpha_{111}P^6 + \alpha_{1111}P^8 - EP + \left(\frac{3}{2}S_{11} + 3S_{12}\right)\sigma_H^2 \quad (27)$$

where $\sigma_H=\sigma_1=\sigma_2=\sigma_3$ is the hydrostatic pressure and $\sigma_H<0$.

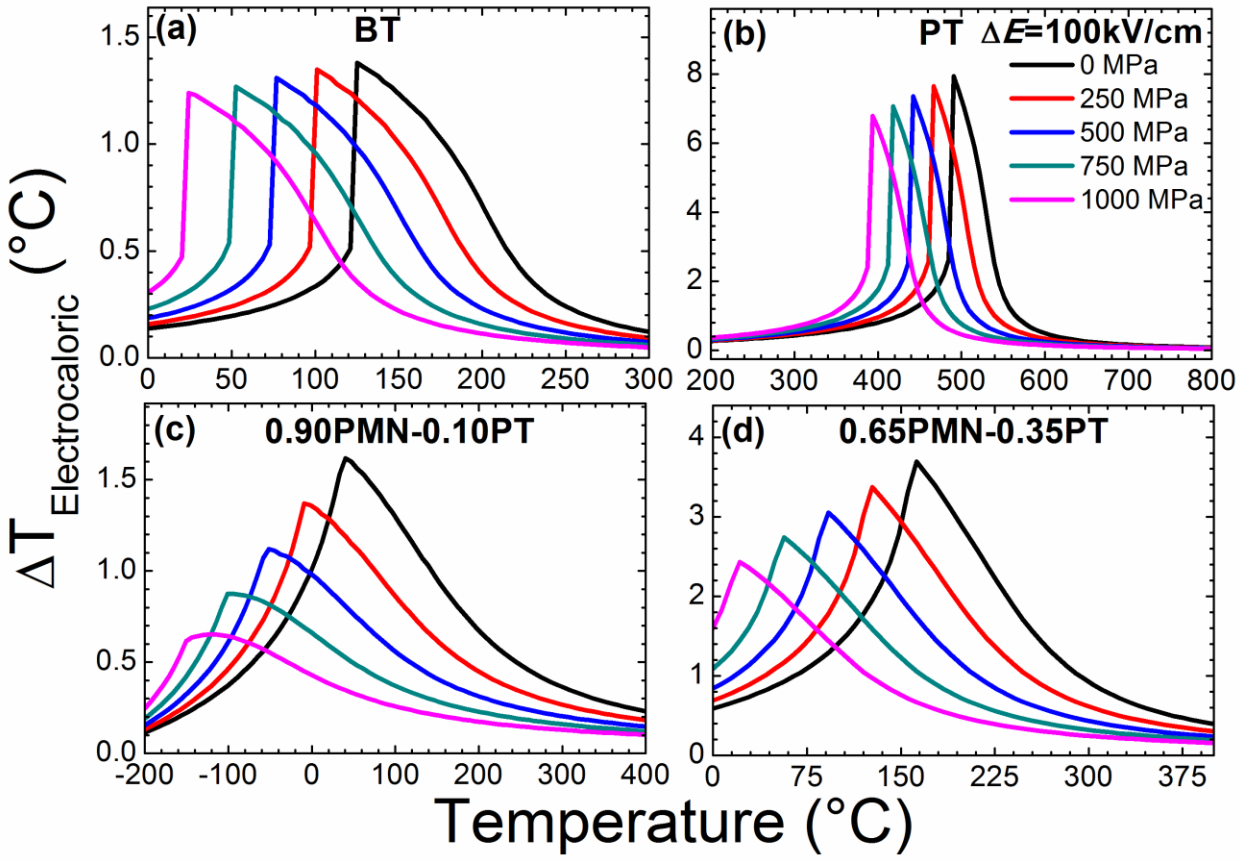

Figure 18– Electrocaloric response under hydrostatic pressure: adiabatic temperature change of BT (a), PT (b), 0.90PMN–0.10P (c), and 0.65PMN–0.35PT (d) as a function of temperature under various magnitudes of hydrostatic pressure. In all cases, hydrostatic pressure shifts the maxima to lower temperatures. This takes place at the cost of decreasing of the magnitude of the maximum value. Electric field is set to be $\Delta E=E_b-E_a$=100 kV/cm with initial field of E_a=0 kV/cm.

In Figure18, we plot the combined σC–EC response for all four materials as functions of T and σ_H. The external electric field difference is set to be $\Delta E=E_b-E_a$=100 kV/cm with an initial (bias) field of E_a=0 kV/cm. As it can be seen, the application of hydrostatic pressure shifts the

peaks of combined σC–EC responses toward lower temperatures due to the suppression of FE transformation, for all four cases. This follows from the relation:

$$\Delta T_C = T_{C(\sigma_H \neq 0)} - T_{C(\sigma_H = 0)} = 4\varepsilon_0 C \sigma_H \left(Q_{11} - Q_{12} \right) \tag{28}$$

which can be obtained by setting α_1-2$Q_{11}\sigma_H$+2$Q_{12}\sigma_H$=0.

For the case of BT, this decrease in T_C is ~100°C for σ_H = 1000 MPa. As such, maximum ΔT_{ad} is near RT but the magnitude of ΔT_{ad} is reduced by 11.3% (from 1.38 to 1.24°C). However, the improvement in the *total* (or *combined*) intrinsic σC–EC response over just the EC adiabatic temperature change is substantial: 1.24°C compared to 0.27°C at RT, respectively. Similar results are observed for PT and the two PMN–PT compositions. The same strategy is not as effective in the case of PT since its bulk T_C is relatively high. Despite that, σC–EC ΔT_{ad} of PT is 0.26 °C at RT and σ_H = 1000 MPa compared to just the EC response which is 0.21°C. For both compositions of PMN–PT, relatively large shifts are observed and this results in high values of σC–EC ΔT_{ad} in the vicinity of RT. For 0.65PMN–0.35PT, the RT σC–EC ΔT_{ad} is 2.4°C for σ_H = 1000 MPa whereas the EC ΔT_{ad} is just 0.71°C.

Discussion & Concluding Remarks

We have computed the combined intrinsic σC and EC properties of four different FE oxides as functions of temperature, applied electric field and stress. Our results show that σC and EC effects can be combined to generate unique proposed refrigeration cycles that employs an external stress and an applied electric field to generate adiabatic temperature changes in FE materials. Uniaxial tensile stresses along the easy axis of polarization in perovskite FEs can significantly shift the PE–FE transition temperature to higher temperatures. This can be utilized to tailor the combined σ–EC response. Also, uniaxial tensile stresses broaden the temperature range at which

relatively high adiabatic temperature changes can be achieved. Considering various investigated systems, among the four materials examined (BT, PT, 0.9PMN–0.10PT, and 0.65PMN–0.35PT), PT displays the highest σC adiabatic temperature change near its T_C (12.7°C at σ=500 MPa). When compared to its pure EC response near T_C (~8°C at ΔE=100 kV/cm), it is 59% higher. Relaxor and relaxor–FE compositions, 0.9PMN–0.10PT and 0.65PMN–0.35PT, exhibit relatively larger adiabatic temperature changes in a wider temperature range and at temperatures closer to RT.

On the other hand, hydrostatic pressure can suppress the transformation to the FE phase. Therefore, it decreases the maximum adiabatic temperature. Meanwhile, it shifts the maximum adiabatic temperature change to lower temperatures that could improve the material performance at RT. We note that, we have limited ourselves to the intrinsic σC–EC response of FE materials. In addition to the intrinsic part of the combined EC properties, these four materials may also exhibit significant *extrinsic* contributions in their caloric responses. This is due to the presence of adaptive polydomain structures, which consist of structural or elastic domains [98, 99]. The extrinsic response is a result of reversible domain wall displacements in the presence of elastic and electric fields [100]. The effect is substantial in hard ferroelectricity such as PZT, which has been demonstrated both experimentally and theoretically [101, 102]. Furthermore, in relaxor–FEs, the extrinsic contribution can be significant near the MPB [103]. This can be attributed to the formation of nanodomains [104–109]. Recent theoretical studies suggest that there is an increase in pyroelectric response of polydomain FE films [89, 110]. These findings are parallel to what is known about extrinsic contribution to piezoelectric properties. In highly piezoelectric FE materials, not only does the electric field affect ionic displacement [54], but also electrostriction *and* reversible domain wall displacement, which should also be considered [55, 111]. Thus, we conclude that such extrinsic contributions could add to the intrinsic response and would potentially

result in relatively large entropy variations in FEs. We note, however, that defects such as dislocations, vacancies, and space charges may smear the FE phase transformation and can result in a degradation of EC properties [112, 113]. And finally, we would like to point out that for optimum combined σ–EC properties, it is perhaps best to concentrate on FEs with second–order phase transformations to avoid hysteretic losses associated with domain nucleation and growth during the polarization switching process. This current study is the first step on the determination of a phase space comprised of materials chemistry, strain, temperature, and electric field to obtain large caloric effects for practical applications.

Flexocaloric Effect

Introduction of Flexoelectric Effect

The flexoelectric response is present in all insulating materials. It results in generation of electric polarization as which is due to presence of inhomogeneous strains or "strain gradients". This phenomenon can occur in crystals with any of the typical symmetry systems. This is due to the fact that strain gradients break inversion symmetry of centrosymmetric crystals as well [18, 114, 115]. Therefore, the flexoelectric effect can be defined as the change in the electric polarization as a function of the strain variations at constant electric field *E*, i.e.,

$$\mu_{klij} = \left(\frac{\partial P_i}{\partial \left(\partial u_{kl} / \partial x_j \right)} \right)_{E=0} \tag{29}$$

where P_i is polarization vector, u_{kl} is the strain tensor, $\partial u_{kl}/\partial x_j$ is the strain gradient and μ_{klij} is the flexoelectric tensor [116]. It has been observed that in linear dielectrics, flexoelectric coefficients are small compared to PEs and FEs. For example, in MgO and NaCl, μ_{11} (in contracted notation) is -111.7 and -62.8 pC/m, respectively [117]. Consequently, it would be difficult to obtain high values of electrical polarization in this type of materials. On the other hand, flexoelectric polarization in FEs can be substantial. This is because of the existing non–centrosymmetric displacements that generate built–in polarization. Therefore, enhanced properties are expected when there is a large strain gradient in a FE material. Physical properties can be altered with this induced strain gradient. For example, Catalan *et al.* suggest significant decreases in the dielectric constant for FE thin films that are subjected to inhomogeneous, in–plane strains [118]. As for centrosymmetric dielectric materials, linear coupling between strain gradient and electric

polarization can lead to large piezoelectric and pyroelectric responses [116, 119–121]. For example, Biancoli *et al*. attribute observed pyroelectric and piezoelectric signals in PE barium strontium titanate samples [119]. They mention that these samples had never been in their FE phase to flexoelectricity. In another example, Chin *et al*. investigated the electro–thermal behavior of PE barium strontium titanate thin films with huge strain gradient in the order of 10^4 m^{-1} due to the lattice mismatch with substrate. Under a heating rate of 0.75 ˚C/s, they report the generation of 86 nW/cm^3 power density with an output voltage of 1.8 mV [121].

Despite the fact that epitaxial thin films can possess much larger magnitudes of strain gradient compared to bulk materials [122], flexoelectric properties are mostly studied in bulk materials, with not many potential applications [123–125]. In the case of FC response, a few studies on FE thin films show promising results [16]. This is perhaps the main reason that there has been extensive work on flexoelectric effects in FE materials [126, 127]. However, for FEs in bulk form, it is difficult to apply inhomogeneous stresses (such as through 3– or 4–point bending or via the tip of an atomic force microscope) that would result in appreciable strain gradients without mechanical failure [121, 122, 128]. For example a maximum strain of 10^{-6} was achieved in $SrTiO_3$ single crystal via oscillatory 3–point bending, resulting in polarizations in the order of 1–10 nC/m [129].

Flexoelectric Effect in Epitaxial Thin–Films

Partially or fully relaxed epitaxial thin films may display strong strain variations across significantly shorter distances. In epitaxial films, internal stresses arise from the lattice mismatch between the film and the substrate. This equi–biaxial strain is homogeneously distributed throughout the volume of the film [130]. It has been shown that if FE films, such strains can result

in changes in the nature of the phase transformation from the PE to the FE state (from first– to second–order), the temperature of the PE–FE transformation [49, 131], physical properties [25], and may even result in the stabilization of phases that do not form in bulk form [132]. The internal stresses in epitaxial films can be relaxed by forming an orthogonal network of misfit dislocations at the film–substrate interface. The interplay between the relaxation of the epitaxial strains that reduces the total energy of the system and the self–energies of the dislocations that have to be generated, results in a critical thickness (h_c) for the formation of interfacial misfit dislocations below which these misfit dislocations are not feasible. The degree of relaxation provided by this network of dislocations depends on parameters such as the film thickness and the total misfit strain energy and is completely reduced for film thicknesses $h >> h_c$. While within the volume of the film average in–plane strains are relieved, there exist strong strains due to the presence of the misfit dislocations in the vicinity of the interface. The change of the strain state from the interface towards the film surface would result in polarization variations via the flexoelectric effect which can be substantial compared to bulk materials due to reduced dimensions in thin film [118, 133, 134].

Experimentally, strain gradients of about 10^7 m^{-1} are measured around dislocations in epitaxial (001) $PbZr_{0.52}Ti_{0.48}O_3$ films grown on (001) $SrRuO_3$–buffered (001) $SrTiO_3$ substrates [135]. Other defects may result in strain gradients as well; for example, epitaxial $HoMnO_3$ FEs under tensile strain of around 5%, display strain variations as large as 10^6 m^{-1} which are believed to be partially due to the presence of oxygen vacancies [133]. We note that strain relaxation can also occur as a result of different growth directions and chemical fluctuations. This has been reported for $(La_{0.7}Sr_{0.3})MnO_3$ epitaxial thin films deposited on $SrTiO_3$ substrates via pulsed laser deposition [136].

Flexocaloric Effect in Epitaxially Strained Thin Films

Can these strain gradients that exist in partially or fully relaxed epitaxial FEs, result in appreciable adiabatic temperature variations? In other words, can the flexoelectric effect provide a FC response? In this study, we show theoretically that the answers to both questions are yes; The FC effect can be substantial and may provide temperature variations of the order of 1°C in prototypical heteroepitaxial FE thin films. We demonstrate that this effect is another channel of entropy variation that can supplement electro– and elastocaloric effects in FEs that can be utilized in on–chip cooling/heating applications [13, 24, 31, 36]. A report of first–principles calculations suggests an adiabatic temperature change of ΔT_{ad}=1.5 °C at 16 °C in $Ba_{0.5}Sr_{0.5}TiO_3$ under a strain gradient of 1.5 μm^{-1} [16].

Misfit Dislocations and Flexocaloric Calculations

We present here a thermodynamic analysis of FC adiabatic temperature change in prototypical epitaxial FE system BT thin films. We take into account strain relaxation through formation of misfit dislocations. In heteroepitaxial films, the internal strain due to lattice mismatch can be relaxed with formation of misfit dislocations [137]. As the misfit dislocations form and accumulate in the film–substrate interface, crystal lattice of the material becomes more and more distorted [16]. Coupling between the stress field of dislocation and the polarization leads to a relaxation in epitaxial thin films [138]. The effective average misfit strain can be derived as [139]:

$$u_m = 1 - \frac{1 - u_m^0}{1 - u_m^0\left(1 - \frac{h_c}{h}\right)} \tag{30}$$

where u_m^0 is the pseudomorphic misfit strain [$= \frac{\left(a_s - a_f\right)}{a_s}$, a_s and a_f are lattice constants of substrate and film respectively], h is the film thickness, and h_c is Matthews–Blakeslee critical thickness for dislocation formation [140, 141]. Figure 19 is an illustration of strain throughout the epitaxially grown films with different film thicknesses. For films with thicknesses smaller than the critical thickness for formation of misfit dislocations ($h<h_c$) the film experiences a uniform strain throughout its bulk (Figure 19(a)). If the film has thickness of higher than hc, misfit dislocations form and help to relax the imposed strain from the substrate. This causes generation of a strain gradient through the thickness of the film. However, for relatively thin films, the number of these dislocations would not be sufficient to lead to a full relaxation (Figure 19(b)). On the other hand, for sufficiently thick films ($h>>h_c$), the number of generated misfit dislocations would be sufficient to fully relax the film (Figure 19(c)). In each case, the magnitude of generated strain gradient is different and the corresponding flexoelectric effect would be different. For the cases where $h<h_c$, there will be no strain gradient and $du/dz=0$ throughout the film (Figure 19(d)). As for the case of films with $h=h_2$, the strain gradient would be substantial. In the case of $h=h_3$ however, the strain gradient would be restricted and full relaxation of the film would limit the magnitude of strain gradient and its corresponding flexoelectric effect (Figure 19(f)).

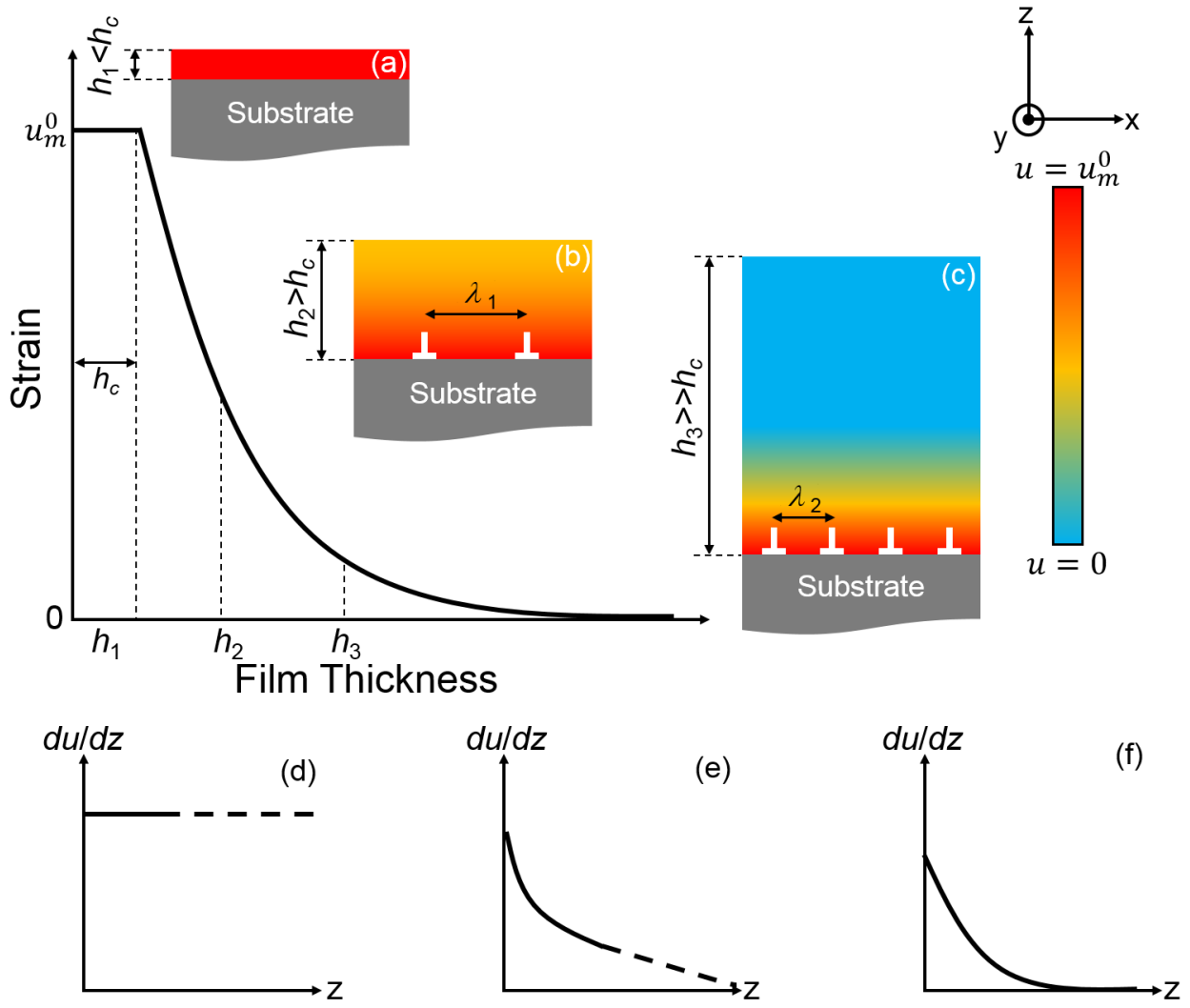

Figure 19– Strain and strain gradient variations: Effective strain throughout film thickness for (a) ultrathin film with thickness smaller than critical thickness for formation of misfit dislocations (h<h_c), (b) mediate film thicknesses and (c) relatively higher thiicknesses where the film fully relaxes after a certain point. (c), (d), and (f) presents the strain gradient throughout the film with thicknesses described in (a), (b), and (c).

Considering formation of misfit dislocations as the only mechanism responsible for relaxation, as we go towards the film surface through the film thickness, the strain along the z direction (orthogonal to the film surface) reads [142]:

$$u\left(z,h_f\right)=u_0\left[\cosh\left(\frac{z}{\delta}\right)-\tanh\left(\frac{h_f}{\delta}\right)\sinh\left(\frac{z}{\delta}\right)\right]+u_t \tag{31}$$

Here δ is an effective depth of penetration for dislocation derived strain. If we combine Equations (30) and (31), for ε_0 we obtain:

$$u_0=\frac{h_f\left(u_{ave}-u_t\right)}{\delta\tanh\left(\frac{h_f}{\delta}\right)} \tag{32}$$

where u_{ave} is average strain in the film and obtain via $u_{ave}=u_m+u_t$. u_t is the thermal strain which is due to the mismatch between thermal expansion coefficients of film and substrate. Knowing the strain variation through the thickness, the strain gradient then is calculated as [142]:

$$\frac{\partial u}{\partial z}=\frac{u_0}{h_f}\left[\cosh\left(\frac{h_f}{\delta}\right)-\tanh\left(\frac{h_f}{\delta}\right)\sinh\left(\frac{h_f}{\delta}\right)-1\right] \tag{33}$$

In Figure20 we show the strain variation as a function of film thickness for different magnitudes of compressive misfit strain. In Figure 20(a) and (b) it can be observed that that as we increase the film thickness, as a general trend for all misfit strains, the value of average strain and the strain gradient decrease. Also, as shown in Figure 20(c) and (d), as we increase the value of compressive misfit strain, regardless of the film thickness, the average stain and the strain gradient both increase.

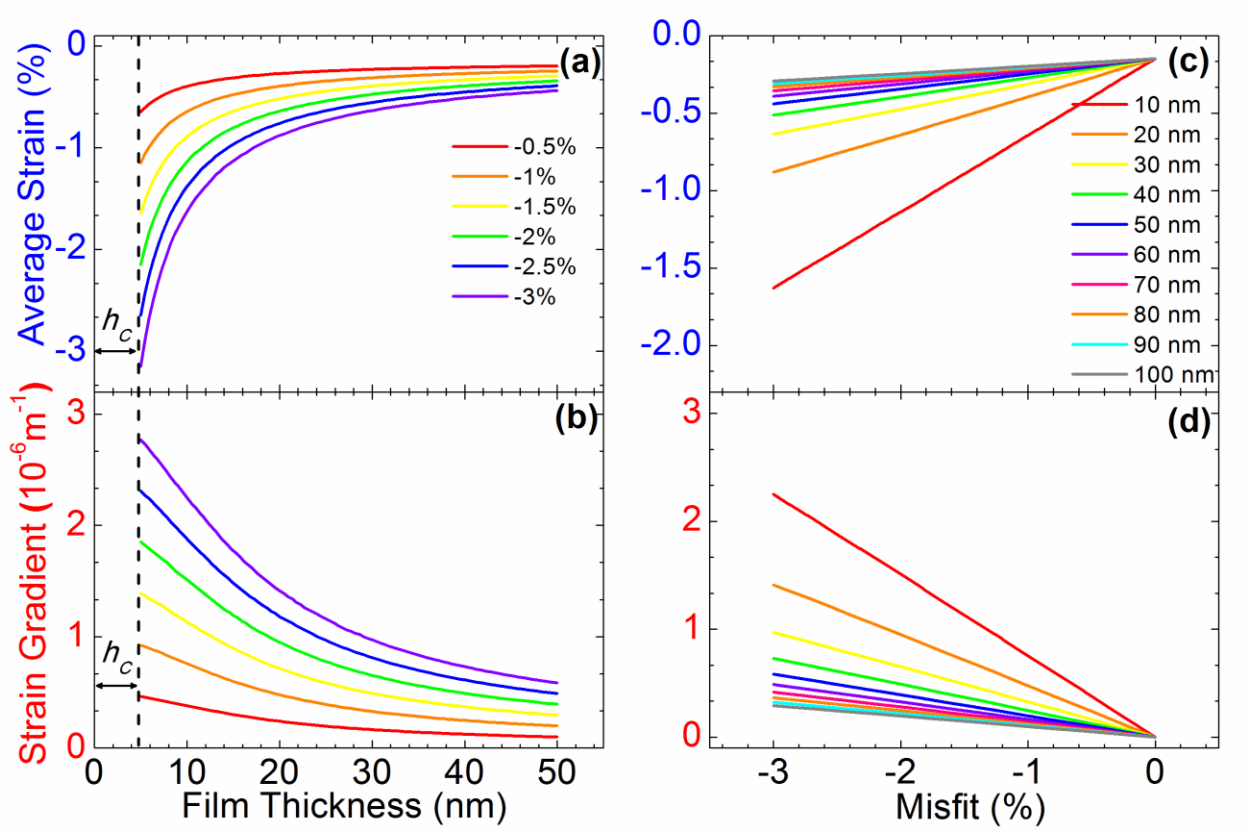

Figure 20– Strain variations: (a) Effective misfit strain throughout film thickness and (b) strain gradient as a function of film thickness at various compressive misfit strains. h_c=5 nm is the Matthews–Blakeslee critical film thickness for formation of misfit dislocations. (c) shows the effective misfit strain and (d) shows strain gradient as a function of compressive misfit strain at various film thickness. Thicker films possess smaller effective misfit strain and strain gradients. Higher misfit stains imposes higher strain gradient and effective misfit strain.

In Figure 21, we take the case for epitaxial BT films epitaxially grown on top of strontium titanate substrates. Ideally, this would give a lattice mismatch of around 2%. We chose three different thicknesses of h=5, 10, and 20nm shown in Figure 21(a), (b), and (c), respectively. As it can be observed, in terms of strain at the interface and also the strain gradient, the thinnest film shows the highest response.

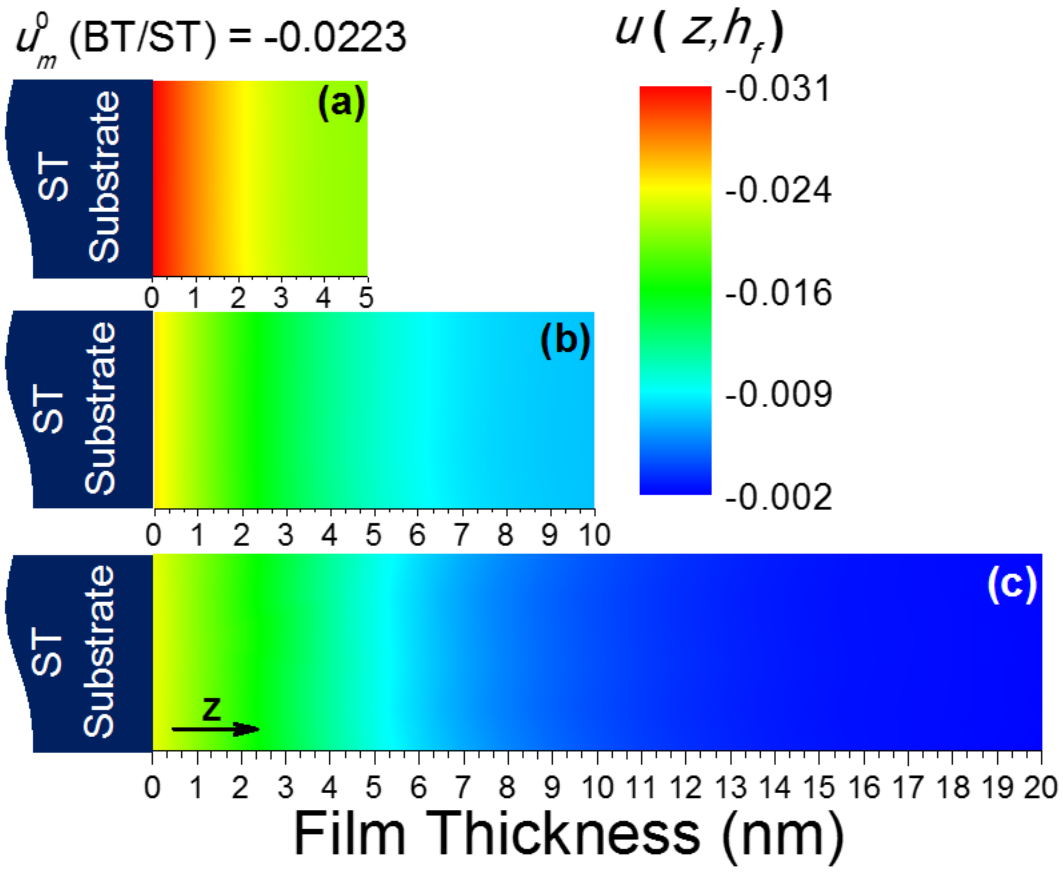

Figure 21– Strain profile of BT/ST system: Strain variation of epitaxial BT on ST substrate with misfit strain of u^0_m =-2.23% at film thicknesses of (a) 5, (b) 10, and (c) 20 nm. As the thickness increases both strain at the film substrate interface and strain gradient decrease.

We consider a (001) monodomain epitaxial film on a thick (001) cubic substrate. We only consider the FE–PE phase transition which simplifies the problem by taking into account only the polarization component along *z* axis. Taking into account the equi–biaxial in–plane misfit strain u_m and flexoelectric effect, the thermodynamic potential of the film *G* in a renormalized form reads [143]:

$$G = \alpha_1^* P^2 + \alpha_{11}^* P^4 + \alpha_{111} P^6 + P\gamma_{ijkl}\frac{d\varepsilon_{jk}}{dz} \tag{34}$$

and renormalized coefficients are given by

$$\alpha_1^* = \alpha_1 - u_m \frac{Q_{11} + Q_{12}}{S_{11} + S_{12}}, \tag{35}$$

$$\alpha_{11}^* = \alpha_{11} \frac{Q_{12}^2}{S_{11} + S_{12}} \tag{36}$$

where P is the polarization along the z axis, $\alpha_1=(T-T_0)/2\varepsilon_0 C$ is the dielectric stiffness (T_0 Curie–Weiss temperature, C constant of a bulk FE, and ε_0 the permittivity of free space), α_{11} and α_{111} are higher order stiffness coefficients, Q_{ij} are the electrostrictive coefficients, and S_{ij} are the elastic compliances of the film in Voigt notation. γ_{ijkl} is the flexoelectric couplings and $d\varepsilon_{jk}/dz$ is the gradient of ε_{jk} component of the strain tensor along z. Kogan *et al*. provided a theoretical estimate of the flexocoupling coefficient [144]. Kogan's estimate considers point charges q in a simple lattice with interatomic spacing a. A distortion of lattice by an atomic–scale strain results in a strain gradient in the order $1/a$. This follows by generation of polarization which would be of order of $(ea)/a^3$. This perturbation then changes the energy density by a factor of $\sim q^2/(4\pi\varepsilon_0 a)\times a^{-3}$. This energy change is equal to the flexoelectric term in Equation (34), $P\gamma\left(\frac{\partial u}{\partial x}\right)$. Solving this equation for γ gives $\gamma \approx \frac{q}{4\pi\varepsilon_0 a}$ [18].

As for the calculation of caloric adiabatic temperature change ($\Delta T_{Caloric}$), we use a formulation proposed by Pirc *et al.* [93] We choose this method instead of the conventional indirect calculation in which $\Delta T_{Caloric}$ is calculated via Maxwell relation derived expression [15, 21]:

$$\Delta T_Y = -\int_{Y_i}^{Y_f} \frac{T}{C_Y}\left(\frac{\partial X}{\partial T}\right)_Y dY \tag{37}$$

In Equation (37), X is an arbitrary extensive variable and Y is its conjugated field. In the Pirc *et al.* method, a general form for entropy of a FE system under a stimuli field F can be written as a sum of polarization dependent dipolar entropy (S_{dip}) and lattice entropy (S_{latt}):

$$S(F,T) = S_{dip}(F,T) + S_{latt}(T) \tag{38}$$

Since polarization of the system changes due to strain gradient, S_{dip} then becomes a field dependent function. Whereas for S_{latt}, changes with field is small and can be ignored. So, it can be safely assumed that S_{latt} is field independent [93]. In our FE configuration, system passes from an initial state (F_i, T_i) to a final state (F_f, T_f). Since total entropy of the system must be zero and entropy is essentially a function of initial and final states, the following relation holds:

$$\Delta S = \left[S_{dip}(F_2,T_2) + S_{latt}(T_2)\right] - \left[S_{dip}(F_1,T_1) + S_{latt}(T_1)\right] = 0 \tag{39}$$

Hence:

$$S_{latt}(T_2) - S_{latt}(T_1) = -\left[S_{dip}(F_2,T_2) - S_{dip}(F_1,T_1)\right] \tag{40}$$

The change in lattice entropy is obtained via:

$$S_{latt}(T_2) - S_{latt}(T_1) = \int_{T_1}^{T_2} \frac{C_{latt}(T)}{T} dT \cong C_{latt}(T_1)\ln\left(\frac{T_2}{T_1}\right) \tag{41}$$

where C_{latt} is the lattice heat capacity of the system per volume. The available experimental data in the literature confirms that C_{latt} can safely be assumed to be a well–behaved weak function of

temperature. [62] Solving Equation (39) for T_2 gives a self–consistent equation to obtain final adiabatic temperature change $\Delta T_{Caloric} = T_2 - T_1$:

$$T_2 = T_1 \exp\left[-\frac{1}{C_{latt}} \left[S_{dip}\left(F_2, T_2\right) - S_{dip}\left(F_1, T_1\right) \right] \right] \tag{42}$$

S_{dip} then can be calculated using energy function (Equation (34)) and the relation $S_{dip} = -\left(\frac{\partial(\Delta G)}{\partial T} \right)_F$. Since in our energy function, in most cases there are two temperature dependent Landau coefficients, the final relation of the self–consistent equation reads:

$$T_2 = T_1 \exp\left[\frac{1}{2C_{latt}} \left[\frac{d\alpha_1}{dT}\left(P^2(F_2,T_2) - P^2(F_1,T_1)\right) + \frac{d\alpha_{11}}{dT}\left(P^2(F_2,T_2) - P^2(F_1,T_1)\right) \right] \right] \tag{43}$$

In Figure 22 we show the adiabatic temperature change of a 20nm BT film as a function of compressive misfit strain at various temperatures. As it can be seen, as the magnitude of compressive misfit strain increases, the maximum FC response shifts towards higher temperatures and its magnitude increases. Regardless, the caloric response at temperatures close to RT improves as the misfit strain increases.

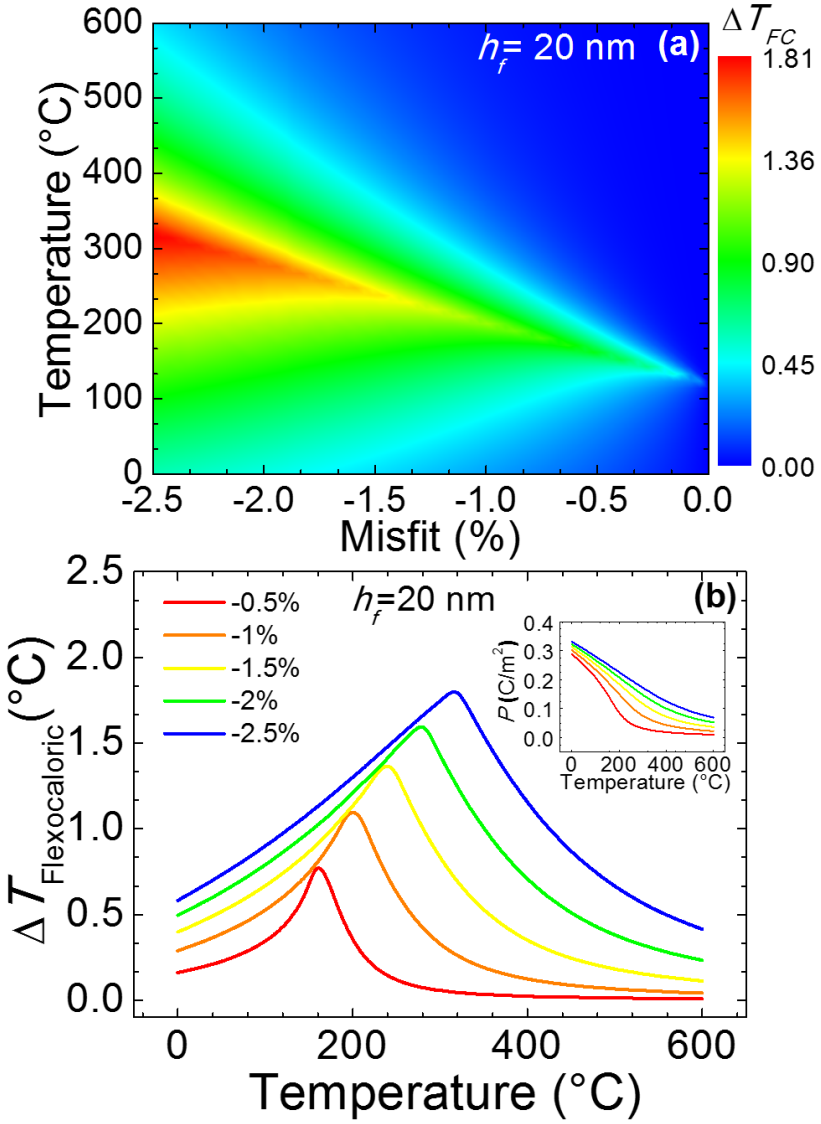

Figure 22– Adiabatic temperature change and misfit strain: (a) Contour plot of adiabatic temperature change at various temperatures and different misfit strains, and (b) adiabatic temperature change variations as a function of temperature at different misfit strains for a 20 nm thick BT. A maximum of ΔT=1.81 °C is calculated at u^0_m =-2.5% at T=310 °C. As increases, the magnitude of the ΔT_{max} increases and the temperature at which it occurs shifts to higher temperatures. The inset in (b) exhibits the polarization variations as u^0_m changes.

Figure 23 presents the FC response of BT films on top of cubic strontium substrates. Here we will lattice mismatches around 2%. While the highest response is atcheived in relatively high temperatures, the smaller thicknesses are evindently promoting the FC response. It is observed in Figure 23(b) that, as the thickness increases, the temperature at which the maximum caloric

response happens shifts towards lower temperatures. However, the magnitude of this maxima drops dramatically. Nevertheless, The FC response improves at temperatures that are in the vicinity of RT.

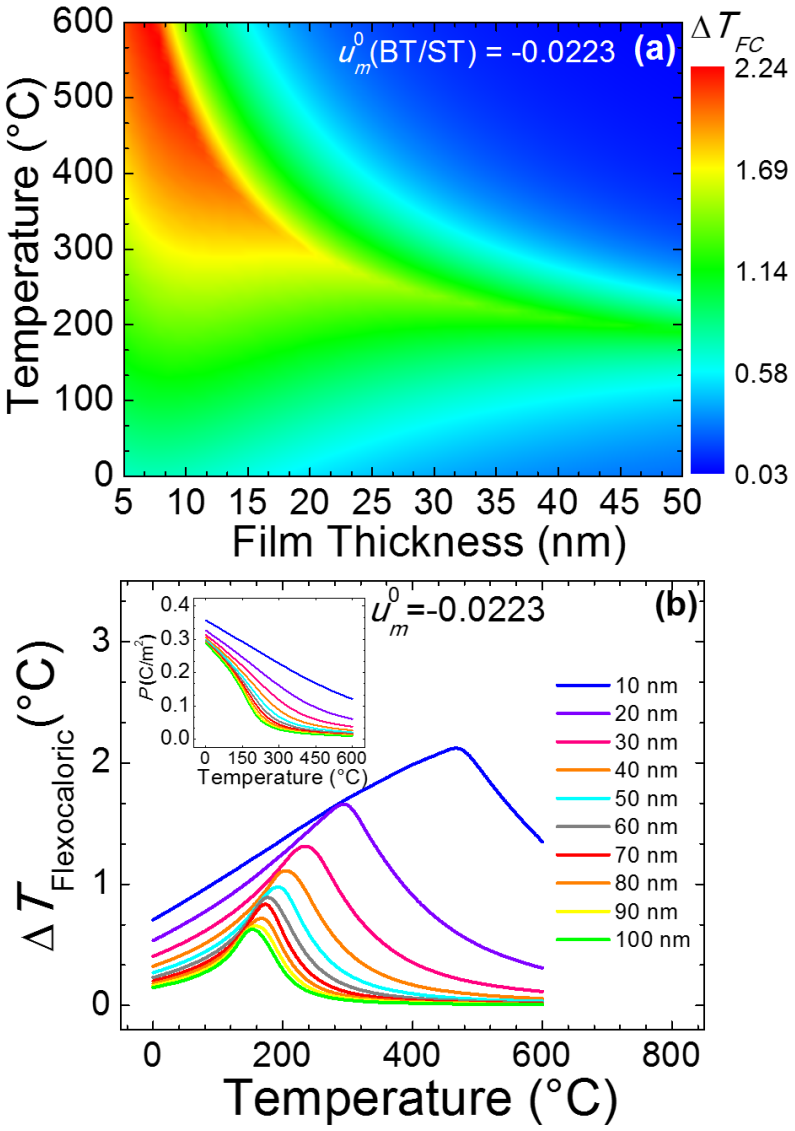

Figure 23– Adiabatic temperature change and film thickness: (a) Contour plot of adiabatic temperature change at various temperatures and different film thicknesses, and (b) adiabatic temperature change variations as a function of temperature at different film thicknesses for a BT on ST substrate with u_m^0 =-2.23%. Maximum values of ΔT occurs at higher temperature and thinner films. As the film thickness increases, the magnitude of the ΔT_{max} decreases and the temperature at which it occurs shifts to lower temperatures. The inset in (b) exhibits the polarization variations as film thickness changes.

Concluding Remarks

Our results show that in epitaxial thin films with compressive misfit strains, the FC effect can be substantial and may provide temperature variations of the order of 1^{o}C in prototypical heteroepitaxial FE thin films. This effect therefore, may be considered as another channel of entropy variation that can supplement electro– and elastocaloric effects in FEs that can be utilized in on–chip cooling/heating applications. In terms of the optimization of the parameters, we predict that as the high thicknesses suppress the FC responses, the compressive misfit strains promote this effect possibly in high effects. We show a strong link between strain relaxation and strain gradients in epitaxial films and its caloric response. Our results also suggest a promising perspective to find solid–state systems with giant caloric responses to be used as alternatives for conventional refrigeration technologies.

CHAPTER 4: SUMMARY AND CONCLUTSION

Multiple driving forces in solid–state materials can be utilized for entropy changes and hence strong caloric responses can be realized. In multiferroic materials, adiabatic temperature changes can be obtained by a combination of various application of electric, stress, and magnetic fields. These external stimuli provide additional channels of entropy variations resulting in a multi–caloric response.

In FE systems, caloric responses can be obtained with the application of electric and mechanical fields. As a result, FE materials are emerging as an ideal material that may host giant EC and/or mC responses close to RT. Here, we investigated the intrinsic EC and mC of prototypical FE materials using Landau–Devonshire theory of phase transformations with appropriate electrical and electro–mechanical boundary conditions.

Electrocaloric Response in Ferroelectric Materials

EC materials have emerged as a viable technology for solid state heating/cooling and waste heat recovery applications. We determined intrinsic EC entropy and temperature changes in perovskite FEs using theoretical tools supported by experimentally measured heat capacities as a function of the applied electric field and temperature. A quantitative analysis of the thermal, pyroelectric and EC properties of representative ceramic FE systems was provided for BT and PT that display a weak and a strong first–order phase transformation to the FE state, and relaxor–FE PMN–PT solid solutions. Our results indicate that the intrinsic adiabatic temperature changes in relaxor–FEs are substantial. Temperature variations (related to reduced entropy) as high as 14 °C can be achieved with applied fields on the order of 1 MV/cm at T~350 °C for (001) oriented 0.65PMN–0.35PT. Moreover, the EC response does not vary over a large temperature interval: 13±1 °C for 200<T<600 °C. In PT, the adiabatic temperature change is approximately 28 °C for an applied field of 1 MV/cm, rivaling the best EC response observed in polymer FEs. This study

provides the general methodology for theoretical analysis to both assess and guide the way in discovering newer high performance EC materials.

Mechanocaloric Response in Ferroelectric Materials

As for the mC effect, the intrinsic σC and stress–mediated EC behavior of prototypical FE materials was computed using Landau–Devonshire theory of phase transformations utilizing appropriate electrical and electro–mechanical boundary conditions. Our results indicated that relatively high combined elasto– and EC adiabatic temperature changes can be obtained in FEs. Furthermore, external stresses allow the maximum electro–elastocaloric response to be tuned towards room temperature. Our calculations also showed that relaxor FEs should exhibit large adiabatic temperature variations in relatively broad temperature ranges.

Flexocaloric Response in Ferroelectric Materials

We also investigated the effect of inhomogeneous strain that potentially allows manifestation of FC effect as another caloric effect that is a stress–driven component. This effect was of especial interest because it could lead to high caloric responses above the Curie point FC response of FE material systems was computed that arise from the generation of strain gradient induced misfit dislocations. The FC response of FE material systems was computed due to generation of strain gradient induced via misfit dislocations. Considering the electromechanical coupling between the polarization and stress gradient, a nonlinear thermodynamic model was employed that took into account the appropriate mechanical boundary conditions. These misfit dislocations result in strong strain variations through the film thickness in epitaxially grown barium titanate. As a result, adiabatic temperature changes over 1.81 °C could be realized in 20 nm thick BT films. We showed a strong link between strain relaxation and strain gradients in epitaxial films

and its caloric response. We note that certain FEs could take advantage of FC effect to be used to produce cooling well even above their Curie temperature if they suitably employ the flexoelectric effect.

These findings indicate that caloric responses in ferroic materials can be deterministically controlled and enhanced by utilizing a variety of external stimuli. Our results suggest a promising perspective to find solid–state systems with giant caloric responses to be used as alternatives for conventional refrigeration technologies.

REFERENCES

[1] X. Moya, S. Kar-Narayan, N. Mathur, Caloric materials near ferroic phase transitions, Nature materials 13(5) (2014) 439-450.
[2] K.A. GschneidnerJr, V. Pecharsky, A. Tsokol, Recent developments in magnetocaloric materials, Reports on Progress in Physics 68(6) (2005) 1479.
[3] J. Scott, Electrocaloric materials, Annual Review of Materials Research 41 (2011) 229-240.
[4] X. Li, S.-G. Lu, X.-Z. Chen, H. Gu, X.-s. Qian, Q. Zhang, Pyroelectric and electrocaloric materials, Journal of Materials Chemistry C 1(1) (2013) 23-37.
[5] L. Manosa, A. Planes, M. Acet, Advanced materials for solid-state refrigeration, Journal of Materials Chemistry A 1(16) (2013) 4925-4936.
[6] Y. Liu, J. Wei, P.-E. Janolin, I.C. Infante, J. Kreisel, X. Lou, B. Dkhil, Prediction of giant elastocaloric strength and stress-mediated electrocaloric effect in BaTiO 3 single crystals, Physical Review B 90(10) (2014) 104107.
[7] Y. Liu, G. Zhang, Q. Li, L. Bellaiche, J.F. Scott, B. Dkhil, Q. Wang, Towards multicaloric effect with ferroelectrics, Physical Review B 94(21) (2016) 214113.
[8] A. Chauhan, S. Patel, R. Vaish, Multicaloric effect in Pb (Mn 1/3 Nb 2/3) O 3-32PbTiO 3 single crystals, Acta Materialia 89 (2015) 384-395.
[9] A. Chauhan, S. Patel, R. Vaish, Elastocaloric effect in ferroelectric ceramics, Applied Physics Letters 106(17) (2015) 172901.
[10] S. Patel, A. Chauhan, R. Vaish, Multiple caloric effects in (Ba0. 865Ca0. 135Zr0. 1089Ti0. 8811Fe0. 01) O3 ferroelectric ceramic, Applied Physics Letters 107(4) (2015) 042902.
[11] S. Lisenkov, I. Ponomareva, Giant elastocaloric effect in ferroelectric Ba 0.5 Sr 0.5 TiO 3 alloys from first-principles, Physical Review B 86(10) (2012) 104103.
[12] M.M. Vopson, Theory of giant-caloric effects in multiferroic materials, Journal of Physics D: Applied Physics 46(34) (2013) 345304.
[13] S. Lisenkov, B. Mani, C.-M. Chang, J. Almand, I. Ponomareva, Multicaloric effect in ferroelectric PbTiO 3 from first principles, Physical Review B 87(22) (2013) 224101.
[14] T. Correia, Q. Zhang, Electrocaloric Materials, Springer2014.
[15] H. Khassaf, J. Mantese, N. Bassiri-Gharb, Z. Kutnjak, S. Alpay, Perovskite ferroelectrics and relaxor-ferroelectric solid solutions with large intrinsic electrocaloric response over broad temperature ranges, Journal of Materials Chemistry C 4(21) (2016) 4763-4769.
[16] S. Patel, A. Chauhan, J. Cuozzo, S. Lisenkov, I. Ponomareva, R. Vaish, Pyro-paraelectric and flexocaloric effects in barium strontium titanate: A first principles approach, Applied Physics Letters 108(16) (2016) 162901.
[17] Y. Liu, J. Wei, P.-E. Janolin, I.C. Infante, X. Lou, B. Dkhil, Giant room-temperature barocaloric effect and pressure-mediated electrocaloric effect in BaTiO3 single crystal, Applied Physics Letters 104(16) (2014) 162904.
[18] P. Zubko, G. Catalan, A.K. Tagantsev, Flexoelectric effect in solids, Annual Review of Materials Research 43 (2013) 387-421.
[19] J. Liu, T. Gottschall, K.P. Skokov, J.D. Moore, O. Gutfleisch, Giant magnetocaloric effect driven by structural transitions, Nature materials 11(7) (2012) 620-626.
[20] V. Provenzano, A.J. Shapiro, R.D. Shull, Reduction of hysteresis losses in the magnetic refrigerant Gd5Ge2Si2 by the addition of iron, Nature 429(6994) (2004) 853-857.

[21] Y. Liu, J.F. Scott, B. Dkhil, Some strategies for improving caloric responses with ferroelectrics, APL Materials 4(6) (2016) 064109.
[22] S. Lu, B. Rožič, Q. Zhang, Z. Kutnjak, X. Li, E. Furman, L.J. Gorny, M. Lin, B. Malič, M. Kosec, Organic and inorganic relaxor ferroelectrics with giant electrocaloric effect, Applied Physics Letters 97(16) (2010) 162904.
[23] S. Fähler, U.K. Rößler, O. Kastner, J. Eckert, G. Eggeler, H. Emmerich, P. Entel, S. Müller, E. Quandt, K. Albe, Caloric effects in ferroic materials: new concepts for cooling, Advanced Engineering Materials 14(1-2) (2012) 10-19.
[24] Y. Liu, I.C. Infante, X. Lou, L. Bellaiche, J.F. Scott, B. Dkhil, Giant Room-Temperature Elastocaloric Effect in Ferroelectric Ultrathin Films, Advanced Materials 26(35) (2014) 6132-6137.
[25] H. Khassaf, N. Khakpash, F. Sun, N. Sbrockey, G. Tompa, T. Kalkur, S. Alpay, Strain engineered barium strontium titanate for tunable thin film resonators, Applied Physics Letters 104(20) (2014) 202902.
[26] D. Damjanovic, Ferroelectric, dielectric and piezoelectric properties of ferroelectric thin films and ceramics, Reports on Progress in Physics 61(9) (1998) 1267.
[27] M.E. Lines, A.M. Glass, Principles and applications of ferroelectrics and related materials, Oxford university press1977.
[28] M.J. Haun, E. Furman, S. Jang, H. McKinstry, L. Cross, Thermodynamic theory of PbTiO3, Journal of Applied Physics 62(8) (1987) 3331-3338.
[29] A.S. Starkov, I.A. Starkov, Giant Piezocaloric Effect in PZT Ceramic Film, Ferroelectrics 483(1) (2015) 102-107.
[30] J.F. Nye, Physical properties of crystals: their representation by tensors and matrices, Oxford university press1985.
[31] A. Mischenko, Q. Zhang, J. Scott, R. Whatmore, N. Mathur, Giant electrocaloric effect in thin-film PbZr0. 95Ti0. 05O3, Science 311(5765) (2006) 1270-1271.
[32] Z. Kutnjak, B. Rožič, R. Pirc, Electrocaloric Effect: Theory, Measurements, and Applications, Wiley Encyclopedia of Electrical and Electronics Engineering (2015).
[33] I. Takeuchi, K. Sandeman, Solid-state cooling with caloric materials, Physics today 68(12) (2015) 48.
[34] S. Alpay, J. Mantese, S. Trolier-McKinstry, Q. Zhang, R.W. Whatmore, Next-generation electrocaloric and pyroelectric materials for solid-state electrothermal energy interconversion, MRS Bulletin 39(12) (2014) 1099-1111.
[35] T. Correia, S. Kar-Narayan, J. Young, J. Scott, N. Mathur, R.W. Whatmore, Q. Zhang, PST thin films for electrocaloric coolers, Journal of Physics D: Applied Physics 44(16) (2011) 165407.
[36] S.G. Lu, Q. Zhang, Electrocaloric Materials for Solid-State Refrigeration, Advanced Materials 21(19) (2009) 1983-1987.
[37] M. Valant, Electrocaloric materials for future solid-state refrigeration technologies, Progress in Materials Science 57(6) (2012) 980-1009.
[38] M. Ožbolt, A. Kitanovski, J. Tušek, A. Poredoš, Electrocaloric refrigeration: thermodynamics, state of the art and future perspectives, international journal of refrigeration 40 (2014) 174-188.
[39] X.S. Qian, S.G. Lu, X. Li, H. Gu, L.C. Chien, Q. Zhang, Large Electrocaloric Effect in a Dielectric Liquid Possessing a Large Dielectric Anisotropy Near the Isotropic–Nematic Transition, Advanced Functional Materials 23(22) (2013) 2894-2898.

[40] X.S. Qian, H.J. Ye, Y.T. Zhang, H. Gu, X. Li, C. Randall, Q. Zhang, Giant electrocaloric response over a broad temperature range in modified BaTiO3 ceramics, Advanced Functional Materials 24(9) (2014) 1300-1305.
[41] B. Neese, B. Chu, S.-G. Lu, Y. Wang, E. Furman, Q. Zhang, Large electrocaloric effect in ferroelectric polymers near room temperature, Science 321(5890) (2008) 821-823.
[42] J. Scott, Applications of modern ferroelectrics, science 315(5814) (2007) 954-959.
[43] R. Ramesh, S. Aggarwal, O. Auciello, Science and technology of ferroelectric films and heterostructures for non-volatile ferroelectric memories, Materials Science and Engineering: R: Reports 32(6) (2001) 191-236.
[44] P. Yudin, A. Tagantsev, Fundamentals of flexoelectricity in solids, Nanotechnology 24(43) (2013) 432001.
[45] F. Jin, G. Auner, R. Naik, N. Schubring, J. Mantese, A. Catalan, A. Micheli, Giant effective pyroelectric coefficients from graded ferroelectric devices, Applied physics letters 73(19) (1998) 2838-2840.
[46] I.A. Kornev, L. Bellaiche, P.-E. Janolin, B. Dkhil, E. Suard, Phase diagram of Pb (Zr, Ti) O 3 solid solutions from first principles, Physical review letters 97(15) (2006) 157601.
[47] J. Lutsko, D. Wolf, S. Yip, S. Phillpot, T. Nguyen, Molecular-dynamics method for the simulation of bulk-solid interfaces at high temperatures, Physical Review B 38(16) (1988) 11572.
[48] S.R. Phillpot, S.B. Sinnott, A. Asthagiri, Atomic-level simulation of ferroelectricity in oxides: Current status and opportunities, Annu. Rev. Mater. Res. 37 (2007) 239-270.
[49] N. Khakpash, H. Khassaf, G. Rossetti Jr, S. Alpay, Misfit strain phase diagrams of epitaxial PMN–PT films, Applied Physics Letters 106(8) (2015) 082905.
[50] K. Bhattacharya, G. Ravichandran, Ferroelectric perovskites for electromechanical actuation, Acta Materialia 51(19) (2003) 5941-5960.
[51] N. Novak, G. Cordoyiannis, Z. Kutnjak, Dielectric and Heat Capacity Study of (Pb (Mg1/3Nb2/3) O3) 0.74-(PbTiO3) 0.26 Ferroelectric Relaxor Near the Cubic-Tetragonal-Rhombohedral Triple Point, Ferroelectrics 428(1) (2012) 43-48.
[52] A. Mischenko, Q. Zhang, R.W. Whatmore, N. Mathur, Giant electrocaloric effect in the thin film relaxor ferroelectric 0.9 PbMg_ (1/3) Nb_ (2/3) O_3-0.1 PbTiO_3 near room temperature, arXiv preprint cond-mat/0604268 (2006).
[53] Y. Zhang, G. Gao, H.L. Chan, J. Dai, Y. Wang, J. Hao, Piezo-Phototronic Effect-Induced Dual-Mode Light and Ultrasound Emissions from ZnS: Mn/PMN–PT Thin-Film Structures, Advanced Materials 24(13) (2012) 1729-1735.
[54] L. Bellaiche, D. Vanderbilt, Intrinsic piezoelectric response in perovskite alloys: PMN-PT versus PZT, Physical review letters 83(7) (1999) 1347.
[55] Y. Sato, T. Hirayama, Y. Ikuhara, Evolution of nanodomains under DC electrical bias in Pb (Mg1/3Nb2/3) O3-PbTiO3: An In-situ transmission electron microscopy study, Applied Physics Letters 100(17) (2012) 172902.
[56] V. Vikhnin, R. Blinc, R. Pirc, Mechanisms of electrostriction and giant piezoelectric effect in relaxor ferroelectrics, Journal of applied physics 93(12) (2003) 9947-9952.
[57] Cooling with Ferroelectric Polymers, Science 321(5890) (2008) 741-741.
[58] G. Zhang, Q. Li, H. Gu, S. Jiang, K. Han, M.R. Gadinski, M.A. Haque, Q. Zhang, Q. Wang, Ferroelectric Polymer Nanocomposites for Room-Temperature Electrocaloric Refrigeration, Advanced Materials 27(8) (2015) 1450-1454.
[59] I. Ponomareva, S. Lisenkov, Bridging the macroscopic and atomistic descriptions of the electrocaloric effect, Physical review letters 108(16) (2012) 167604.

[60] R. Pirc, Z. Kutnjak, R. Blinc, Q. Zhang, Upper bounds on the electrocaloric effect in polar solids, Applied Physics Letters 98(2) (2011) 1909.
[61] G. Akcay, S. Alpay, G. Rossetti Jr, J. Scott, Influence of mechanical boundary conditions on the electrocaloric properties of ferroelectric thin films, Journal of Applied Physics 103(2) (2008) 024104.
[62] N. Novak, Z. Kutnjak, R. Pirc, High-resolution electrocaloric and heat capacity measurements in barium titanate, EPL (Europhysics Letters) 103(4) (2013) 47001.
[63] J. Zhang, A. Heitmann, S. Alpay, G. Rossetti Jr, Electrothermal properties of perovskite ferroelectric films, Journal of materials science 44(19) (2009) 5263-5273.
[64] A.A. BOKOV, Z.-G. YE, Dielectric relaxation in relaxor ferroelectrics, Journal of Advanced Dielectrics 2(02) (2012) 1241010.
[65] L. Garten, P. Lam, D. Harris, J.-P. Maria, S. Trolier-McKinstry, Residual ferroelectricity in barium strontium titanate thin film tunable dielectrics, Journal of Applied Physics 116(4) (2014) 044104.
[66] A.A. Heitmann, G.A. Rossetti, Thermodynamics of ferroelectric solid solutions with morphotropic phase boundaries, Journal of the American Ceramic Society 97(6) (2014) 1661-1685.
[67] D. Damjanovic, A morphotropic phase boundary system based on polarization rotation and polarization extension, Applied Physics Letters 97(6) (2010) 062906.
[68] D. Damjanovic, M. Demartin, Contribution of the irreversible displacement of domain walls to the piezoelectric effect in barium titanate and lead zirconate titanate ceramics, Journal of Physics: Condensed Matter 9(23) (1997) 4943.
[69] D. Lin, S. Zhang, Z. Li, F. Li, Z. Xu, S. Wada, J. Luo, T.R. Shrout, Domain size engineering in tetragonal Pb (In1/2Nb1/2) O3-Pb (Mg1/3Nb2/3) O3-PbTiO3 crystals, Journal of applied physics 110(8) (2011) 084110.
[70] A. Heitmann, G. Rossetti Jr, Thermodynamics of Ferroelectric Solid Solutions with Morphotropic Phase Boundaries, Journal of the American Ceramic Society 97(6) (2014) 16611685.
[71] Z. Kutnjak, J. Petzelt, R. Blinc, The giant electromechanical response in ferroelectric relaxors as a critical phenomenon, Nature 441(7096) (2006) 956-959.
[72] G. Sebald, L. Seveyrat, D. Guyomar, L. Lebrun, B. Guiffard, S. Pruvost, Electrocaloric and pyroelectric properties of 0.75 Pb (Mg1⁄ 3Nb2⁄ 3) O3–0.25 PbTiO3 single crystals, Journal of applied physics 100(12) (2006) 124112.
[73] D. Guyomar, G. Sebald, B. Guiffard, L. Seveyrat, Ferroelectric electrocaloric conversion in 0.75 (PbMg1/3Nb2/3O3)–0.25 (PbTiO3) ceramics, Journal of Physics D: Applied Physics 39(20) (2006) 4491.
[74] N. Novak, R. Pirc, M. Wencka, Z. Kutnjak, High-resolution calorimetric study of Pb (Mg 1/3 Nb 2/3) O 3 single crystal, Physical review letters 109(3) (2012) 037601.
[75] R. Pirc, B. Rožič, J. Koruza, B. Malič, Z. Kutnjak, Negative electrocaloric effect in antiferroelectric PbZrO3, EPL (Europhysics Letters) 107(1) (2014) 17002.
[76] E. Brück, Developments in magnetocaloric refrigeration, Journal of Physics D: Applied Physics 38(23) (2005) R381.
[77] C. Chluba, W. Ge, R.L. de Miranda, J. Strobel, L. Kienle, E. Quandt, M. Wuttig, Ultralow-fatigue shape memory alloy films, Science 348(6238) (2015) 1004-1007.
[78] E. Bonnot, R. Romero, L. Manosa, E. Vives, A. Planes, Elastocaloric effect associated with the martensitic transition in shape-memory alloys, Physical review letters 100(12) (2008) 125901.

[79] L. Mañosa, D. González-Alonso, A. Planes, E. Bonnot, M. Barrio, J.-L. Tamarit, S. Aksoy, M. Acet, Giant solid-state barocaloric effect in the Ni-Mn-In magnetic shape-memory alloy, Nature materials 9(6) (2010) 478-481.
[80] H. Khassaf, N. Khakpash, S. Vijayan, M. Aindow, S. Alpay, Electrostatically driven dielectric anomaly in mesoscopic ferroelectric–paraelectric bilayers, Acta Materialia 105 (2016) 68-74.
[81] S.P. Alpay, J. Mantese, S. Trolier-McKinstry, Q. Zhang, R.W. Whatmore, Next-generation electrocaloric and pyroelectric materials for solid-state electrothermal energy interconversion, MRS Bulletin 39(12) (2014) 1099-1111.
[82] F.-C. Sun, A.M. Dongare, A.D. Asandei, S. Pamir Alpay, S. Nakhmanson, Temperature dependent structural, elastic, and polar properties of ferroelectric polyvinylidene fluoride (PVDF) and trifluoroethylene (TrFE) copolymers, Journal of Materials Chemistry C 3(32) (2015) 8389-8396.
[83] J. Zhang, J.C. Agar, L.W. Martin, Structural phase diagram and pyroelectric properties of free-standing ferroelectric/non-ferroelectric multilayer heterostructures, Journal of Applied Physics 118(24) (2015) 244101.
[84] J. Mangeri, K.C. Pitike, S.P. Alpay, S. Nakhmanson, Amplitudon and phason modes of electrocaloric energy interconversion, npj Computational Materials 2 (2016) 16020.
[85] G.G. Guzman-Verri, P.B. Littlewood, Why is the electrocaloric effect so small in ferroelectrics?, APL Materials 4(6) (2016) 064106.
[86] S. Lu, B. Rožič, Q. Zhang, Z. Kutnjak, R. Pirc, M. Lin, X. Li, L. Gorny, Comparison of directly and indirectly measured electrocaloric effect in relaxor ferroelectric polymers, Applied Physics Letters 97(20) (2010) 202901.
[87] F. Auricchio, R.L. Taylor, Shape-memory alloys: modelling and numerical simulations of the finite-strain superelastic behavior, Computer methods in applied mechanics and engineering 143(1) (1997) 175-194.
[88] A. Lai, Z. Du, C.L. Gan, C.A. Schuh, Shape memory and superelastic ceramics at small scales, Science 341(6153) (2013) 1505-1508.
[89] T. Tong, J. Karthik, R. Mangalam, L.W. Martin, D.G. Cahill, Reduction of the electrocaloric entropy change of ferroelectric PbZr 1− x Ti x O 3 epitaxial layers due to an elastocaloric effect, Physical Review B 90(9) (2014) 094116.
[90] S. Lisenkov, B. Mani, J. Cuozzo, I. Ponomareva, Highly tunable piezocaloric effect in antiferroelectric PbZrO 3, Physical Review B 93(6) (2016) 064108.
[91] B. Rožič, H. Uršič, J. Holc, M. Kosec, Z. Kutnjak, Direct measurements of the Electrocaloric effect in Substrate-Free PMN-0.35 PT thick films on a Platinum layer, Integrated Ferroelectrics 140(1) (2012) 161-165.
[92] M. Davis, D. Damjanovic, N. Setter, Pyroelectric properties of (1-x) Pb (Mg1/3Nb2/3) O3-xPbTiO3 and (1-x) Pb (Zn1/3Nb2/3) O3-xPbTiO3 single crystals measured using a dynamic method, Journal of applied physics 96 (2004) 2811-2815.
[93] R. Pirc, Z. Kutnjak, R. Blinc, Q. Zhang, Electrocaloric effect in relaxor ferroelectrics, arXiv preprint arXiv:1010.2914 (2010).
[94] G. Akcay, S. Alpay, J. Mantese, G. Rossetti, Magnitude of the intrinsic electrocaloric effect in ferroelectric perovskite thin films at high electric fields, Applied physics letters 90(25) (2007) 2909.
[95] G.A. Rossetti Jr, L.E. Cross, K. Kushida, Stress induced shift of the Curie point in epitaxial PbTiO3 thin films, Applied physics letters 59(20) (1991) 2524-2526.

[96] N. Pertsev, A. Zembilgotov, A. Tagantsev, Effect of mechanical boundary conditions on phase diagrams of epitaxial ferroelectric thin films, Physical review letters 80(9) (1998) 1988.
[97] M. Vrabelj, H. Uršič, Z. Kutnjak, B. Rožič, S. Drnovšek, A. Benčan, V. Bobnar, L. Fulanović, B. Malič, Large electrocaloric effect in grain-size-engineered 0.9 Pb (Mg 1/3 Nb 2/3) O 3–0.1 PbTiO 3, Journal of the European ceramic society 36(1) (2016) 75-80.
[98] J. Slutsker, A. Artemev, A.L. Roytburd, Engineering of elastic domain structures in a constrained layer, Acta materialia 52(6) (2004) 1731-1742.
[99] S. Alpay, V. Nagarajan, L. Bendersky, M. Vaudin, S. Aggarwal, R. Ramesh, A. Roytburd, Effect of the electrode layer on the polydomain structure of epitaxial PbZr0. 2Ti0. 8O3 thin films, Journal of applied physics 85(6) (1999) 3271-3277.
[100] R. Xu, J. Zhang, Z. Chen, L.W. Martin, Orientation-dependent structural phase diagrams and dielectric properties of PbZr 1− x Ti x O 3 polydomain thin films, Physical Review B 91(14) (2015) 144106.
[101] P.-E. Janolin, Strain on ferroelectric thin films, Journal of materials science 44(19) (2009) 5025-5048.
[102] N. Pertsev, G. Arlt, A. Zembilgotov, Prediction of a giant dielectric anomaly in ultrathin polydomain ferroelectric epitaxial films, Physical review letters 76(8) (1996) 1364.
[103] N.B. Gharb, S. Trolier-McKinstry, Dielectric nonlinearity of Pb (Yb 1⁄2 Nb 1⁄2) O 3–PbTiO 3 thin films with {100} and {111} crystallographic orientation, Journal of applied physics 97(6) (2005) 064106.
[104] G.A. Rossetti Jr, A.G. Khachaturyan, Inherent nanoscale structural instabilities near morphotropic boundaries in ferroelectric solid solutions, Applied Physics Letters 91(7) (2007) 072909.
[105] A.L. Roytburd, Thermodynamics of polydomain heterostructures. I. Effect of macrostresses, Journal of applied physics 83(1) (1998) 228-238.
[106] N. Pertsev, A. Zembilgotov, Energetics and geometry of 90° domain structures in epitaxial ferroelectric and ferroelastic films, Journal of applied physics 78(10) (1995) 6170-6180.
[107] V. Nagarajan, A. Roytburd, A. Stanishevsky, S. Prasertchoung, T. Zhao, L. Chen, J. Melngailis, O. Auciello, R. Ramesh, Dynamics of ferroelastic domains in ferroelectric thin films, Nature materials 2(1) (2003) 43-47.
[108] J. Ouyang, A. Roytburd, Theoretical modeling of coexisting tetragonal and rhombohedral heterophase polydomain structures in lead zirconate titanate ferroelectric films near the morphotropic phase boundary, Acta materialia 54(20) (2006) 5565-5572.
[109] K.A. Schönau, L.A. Schmitt, M. Knapp, H. Fuess, R.-A. Eichel, H. Kungl, M.J. Hoffmann, Nanodomain structure of Pb [Zr 1− x Ti x] O 3 at its morphotropic phase boundary: investigations from local to average structure, Physical Review B 75(18) (2007) 184117.
[110] T. Tong, J. Karthik, L.W. Martin, D.G. Cahill, Secondary effects in wide frequency range measurements of the pyroelectric coefficient of Ba 0.6 Sr 0.4 TiO 3 and PbZr 0.2 Ti 0.8 O 3 epitaxial layers, Physical Review B 90(15) (2014) 155423.
[111] J. Karthik, L. Martin, Effect of domain walls on the electrocaloric properties of Pb (Zr1− x, Tix) O3 thin films, Applied Physics Letters 99(3) (2011) 032904.
[112] A.P. Levanyuk, I. Misirlioglu, Phase transitions in ferroelectric-paraelectric superlattices, Journal of Applied Physics 110(11) (2011) 114109.
[113] I. Misirlioglu, M. Okatan, S. Alpay, Asymmetric hysteresis loops and smearing of the dielectric anomaly at the transition temperature due to space charges in ferroelectric thin films, Journal of Applied Physics 108(3) (2010) 034105.

[114] A. Tagantsev, Piezoelectricity and flexoelectricity in crystalline dielectrics, Physical Review B 34(8) (1986) 5883.
[115] A.S. Starkov, I.A. Starkov, Impact of the flexocaloric effect on polarization in the flexoelectric layer, International Journal of Solids and Structures 82 (2016) 65-69.
[116] L.E. Cross, Flexoelectric effects: Charge separation in insulating solids subjected to elastic strain gradients, Frontiers of Ferroelectricity, Springer2006, pp. 53-63.
[117] J. Hong, D. Vanderbilt, First-principles theory and calculation of flexoelectricity, Physical Review B 88(17) (2013) 174107.
[118] G. Catalan, L. Sinnamon, J. Gregg, The effect of flexoelectricity on the dielectric properties of inhomogeneously strained ferroelectric thin films, Journal of Physics: Condensed Matter 16(13) (2004) 2253.
[119] A. Biancoli, C.M. Fancher, J.L. Jones, D. Damjanovic, Breaking of macroscopic centric symmetry in paraelectric phases of ferroelectric materials and implications for flexoelectricity, Nature materials 14(2) (2015) 224-229.
[120] L.E. Cross, Flexoelectric effects: Charge separation in insulating solids subjected to elastic strain gradients, Journal of Materials Science 41(1) (2006) 53-63.
[121] H.-A. Chin, S. Mao, C.-T. Huang, K.K. Ohemeng, S. Wagner, P.K. Purohit, M.C. McAlpine, Pyro-paraelectricity, Extreme Mechanics Letters 2 (2015) 20-27.
[122] D. Lee, T.W. Noh, Giant flexoelectric effect through interfacial strain relaxation, Philosophical Transactions of the Royal Society of London A: Mathematical, Physical and Engineering Sciences 370(1977) (2012) 4944-4957.
[123] W. Ma, L.E. Cross, Flexoelectric polarization of barium strontium titanate in the paraelectric state, Applied Physics Letters 81 (2002) 3440-3442.
[124] W. Ma, L.E. Cross, Large flexoelectric polarization in ceramic lead magnesium niobate, Applied Physics Letters 79(26) (2001) 4420-4422.
[125] W. Ma, L.E. Cross, Flexoelectricity of barium titanate, Applied Physics Letters 88(23) (2006) 2902.
[126] W. Ma, L.E. Cross, Flexoelectric effect in ceramic lead zirconate titanate, Applied Physics Letters 86(7) (2005) 072905.
[127] W. Ma, L.E. Cross, Observation of the flexoelectric effect in relaxor Pb (Mg 1/3 Nb 2/3) O 3 ceramics, Applied Physics Letters 78(19) (2001) 2920-2921.
[128] T.D. Nguyen, S. Mao, Y.W. Yeh, P.K. Purohit, M.C. McAlpine, Nanoscale flexoelectricity, Advanced Materials 25(7) (2013) 946-974.
[129] P. Zubko, G. Catalan, A. Buckley, P. Welche, J. Scott, Strain-gradient-induced polarization in SrTiO 3 single crystals, Physical Review Letters 99(16) (2007) 167601.
[130] J. Wang, J. Neaton, H. Zheng, V. Nagarajan, S. Ogale, B. Liu, D. Viehland, V. Vaithyanathan, D. Schlom, U. Waghmare, Epitaxial BiFeO3 multiferroic thin film heterostructures, Science 299(5613) (2003) 1719-1722.
[131] G. Catalan, B. Noheda, J. McAneney, L. Sinnamon, J. Gregg, Strain gradients in epitaxial ferroelectrics, Physical Review B 72(2) (2005) 020102.
[132] F. Sun, H. Khassaf, S. Alpay, Strain engineering of piezoelectric properties of strontium titanate thin films, Journal of Materials Science 49(17) (2014) 5978-5985.
[133] D. Lee, A. Yoon, S. Jang, J.-G. Yoon, J.-S. Chung, M. Kim, J. Scott, T. Noh, Giant flexoelectric effect in ferroelectric epitaxial thin films, Physical Review Letters 107(5) (2011) 057602.

[134] K.J. Choi, M. Biegalski, Y. Li, A. Sharan, J. Schubert, R. Uecker, P. Reiche, Y. Chen, X. Pan, V. Gopalan, Enhancement of ferroelectricity in strained BaTiO3 thin films, Science 306(5698) (2004) 1005-1009.
[135] V. Nagarajan, C. Jia, H. Kohlstedt, R. Waser, I. Misirlioglu, S. Alpay, R. Ramesh, Misfit dislocations in nanoscale ferroelectric heterostructures, Applied Physics Letters 86(19) (2005) 192910-192910.
[136] J.-L. Maurice††, F. Pailloux‡‡, A. Barthélémy, O. Durand, D. Imhoff, R. Lyonnet, A. Rocher, J.-P. Contour, Strain relaxation in the epitaxy of La2/3Sr1/3MnO3 grown by pulsed-laser deposition on SrTiO3 (001), Philosophical Magazine 83(28) (2003) 3201-3224.
[137] S. Stemmer, S. Streiffer, F. Ernst, M. Rühle, Dislocations in PbTiO3 thin films, physica status solidi (a) 147(1) (1995) 135-154.
[138] S. Alpay, I. Misirlioglu, V. Nagarajan, R. Ramesh, Can interface dislocations degrade ferroelectric properties?, Applied physics letters 85(11) (2004) 2044-2046.
[139] Q. Qiu, V. Nagarajan, S. Alpay, Film thickness versus misfit strain phase diagrams for epitaxial PbTiO 3 ultrathin ferroelectric films, Physical Review B 78(6) (2008) 064117.
[140] J. Matthews, A. Blakeslee, Defects in epitaxial multilayers: I. Misfit dislocations, Journal of Crystal Growth 27 (1974) 118-125.
[141] J. Speck, W. Pompe, Domain configurations due to multiple misfit relaxation mechanisms in epitaxial ferroelectric thin films. I. Theory, Journal of applied physics 76(1) (1994) 466-476.
[142] L. Nicola, E. Van der Giessen, M.E. Gurtin, Effect of defect energy on strain-gradient predictions of confined single-crystal plasticity, Journal of the Mechanics and Physics of Solids 53(6) (2005) 1280-1294.
[143] Z.-G. Ban, S. Alpay, Phase diagrams and dielectric response of epitaxial barium strontium titanate films: A theoretical analysis, Journal of Applied Physics 91(11) (2002) 9288-9296.
[144] S.M. Kogan, Piezoelectric effect during inhomogeneous deformation and acoustic scattering of carriers in crystals, Soviet Physics-Solid State 5(10) (1964) 2069-2070.